Taylor & Francis
Taylor & Francis Group

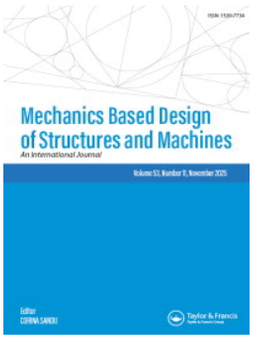

Mechanics Based Design of Structures and Machines
An International Journal

ISSN: 1539-7734 (Print) 1539-7742 (Online) Journal homepage: www.tandfonline.com/journals/lmbd20

# Interaction of stress distribution and stringer slenderness on buckling of stiffened composite elliptical cylindrical shell under axial compression

Davood Poorveis, Amin Khajehdezfuly, Mohammad Reza Sardari & Shapour Moradi

**To cite this article:** Davood Poorveis, Amin Khajehdezfuly, Mohammad Reza Sardari & Shapour Moradi (17 Nov 2025): Interaction of stress distribution and stringer slenderness on buckling of stiffened composite elliptical cylindrical shell under axial compression, Mechanics Based Design of Structures and Machines, DOI: 10.1080/15397734.2025.2585351

**To link to this article:** https://doi.org/10.1080/15397734.2025.2585351

Published online: 17 Nov 2025.

MECHANICS BASED DESIGN OF STRUCTURES AND MACHINES
https://doi.org/10.1080/15397734.2025.2585351



# Interaction of stress distribution and stringer slenderness on buckling of stiffened composite elliptical cylindrical shell under axial compression

Davood Poorveis[a], Amin Khajehdezfuly[a], Mohammad Reza Sardari[a], and Shapour Moradi[b]

[a]Department of Civil Engineering, Faculty of Civil Engineering and Architecture, Shahid Chamran University of Ahvaz, Ahvaz, Iran; [b]Department of Mechanical Engineering, Faculty of Engineering, Shahid Chamran University of Ahvaz, Ahvaz, Iran

**ABSTRACT**

This article investigates the impact of interaction of stress distribution and stringer slenderness on the buckling of stiffened composite elliptical cylindrical shell under axial compression, an important factor that has received limited attention in previous research. Using the finite strip method (FSM), the study introduces a novel approach to simulate stringer-stiffened composite cylindrical shell with elliptical cross section, explicitly incorporating three distinct pre-buckling stress distribution scenarios in the model. Through a parametric study, the research provides nuanced insights into the relationship between stress distribution during pre-buckling analysis and the resulting buckling load of composite cylindrical shells. In this study, various geometric characteristics, including the depth and number of stringers, stringer area index, composite layup, length, and cross-section of the shell, have been examined. By addressing this gap in understanding, the findings contribute valuable knowledge to the design and analysis of stiffened composite shells, offering practical implications for engineering applications.

**ARTICLE HISTORY**
Received 6 March 2025
Accepted 30 October 2025

**KEYWORDS**
Axial buckling load; composite elliptical cylindrical shells; finite strip method; pre-buckling stress; stringer slenderness

## 1. Introduction

Cylindrical shells are wieldy used in different industries by dint their high strength and low weight (Lai et al. 2023; Vu et al. 2023; Shahgholian-Ghahfarokhi, Safarpour, and Rahimi 2021; Nguyen et al. 2024). A review of the literature shows that cylindrical shells are vulnerable to buckling when subjected to different types of loading due to their low thickness to length ratio (Golchi, Talebitooti, and Talebitooti 2019; Xin et al. 2011; Tornabene and Viola 2009). So, numerous studies have been carried out on the effect of different parameters on the buckling behavior of cylindrical shells. In this regard, several techniques have been used to analysis cylindrical shells under different types of loading (Asadi and Qatu 2012). Finite strip method (FSM) is known as one of the most conventional approaches for simulating cylindrical shells (Ovesy and Fazilati 2012). For instance, Ovesy and Fazilati (2012) simulated composite shell using FSM and investigated its free vibration. Silvestre (2008) developed formulation of generalized beam theory to investigate effects of different parameters on the buckling behavior of elliptical cylindrical shells and tubes under compression. Salahshour and Fallah (2018) studied elastic collapse of thin

CONTACT Davood Poorveis dpoorveis@scu.ac.ir Department of Civil Engineering, Faculty of Civil Engineering and Architecture, Shahid Chamran University of Ahvaz, Ahvaz, Iran

long cylindrical shells under external pressure using smeared method. Nguyen et al. (2023) developed an analytical approach for nonlinear buckling analysis of shell segments with graphene-reinforced polymer coating.

Longitudinal and circumferential stiffeners (i.e., stringers and rings) are used to enhance the buckling load of the shell. Zhang et al. (2024) conducted experimental and numerical investigations on buckling of composite stiffened panel under axial compression. A review of the literature shows that stiffened shells are generally modeled through two main approaches including the smeared method and the discrete method. The smeared method, also known as the equivalent shell method, does not model the stiffeners explicitly or independently (Nguyen, Elishakoff, and Nguyen 2009). Instead, based on the number, spacing, and depth of the stringers, an equivalent shell with increased thickness is developed to simulate a shell with equivalent stiffness to the original stiffened shell. In the most of studies carried out on the buckling of stiffened shells, the stiffened shell was simulated as an equivalent shell without considering the stringers in the model (Dung and Hoa 2013; Wang et al. 2021). For instance, Duc, Nguyen, and Khoa (2017) investigated the effects of stiffeners, elastic foundation, temperature gradient, and shell geometry properties on the nonlinear dynamic vibration and behavior of functionally graded material (FGM) stiffened elliptical cylindrical shell through smeared approach. The smeared approach is particularly suitable for the shells stiffened with a large number of shallow stringers having uniform spacing (i.e., when the stringer depth is not significantly larger than the shell thickness, the stringers is a shallow stringer). In the smeared approach, the effect of stringers on the buckling of stringer stiffened shells is indirectly considered in the simulation and so, the behavior of stringers is not considered and investigated individually (Duc et al. 2016).

In contrast, the stiffened shell model developed through discrete method includes two main components: shell and stringers. Importantly, within this method, two modeling strategies exist depending on how the interaction between the shell and the stiffeners is defined. In the first strategy of discrete method, which is commonly used in the literature, deformation of the stiffeners (displacements and rotations) is derived from the shell deformation, based on the assumption of full compatibility between shell and stringers (Kabir and Poorveis 2006). The total degrees of freedom of the model developed in this approach is same as that of the smeared one. However, unlike the smeared method, this approach accounts for considering the exact position of each stiffener in the stiffened shell model, applying effect of stringers to the shell at their corresponding locations. Therefore, when the stiffener spacing varies along the shell perimeter (stringers with non-uniform spacing), this method can yield a more accurate representation of the stiffened shell and provide more precise buckling load predictions. For instance, Sadeghifar, Bagheri, and Jafari (2011) and Sadeghifar, Bagheri, and Jafari (2010) developed a model of stringer-stiffened cylindrical shell and investigated the effects of cross-section, thickness, position, and number of stringers on the buckling load of the shell. Bich et al. (2013) investigated the nonlinear static and dynamic buckling behaviors of stringer-stiffened thin FGM shell under axial compression by simulating shell and different types of stringers in their study. Ghorbanpour Arani et al. (2010) utilized the Ritz method to study elastic buckling of ring and stringer-stiffened cylindrical shells under general pressure and axial compression.

In the second strategy of discrete approach (advanced discrete approach), the displacements and rotations of the stiffeners are treated separately and independently from the shell (Poorveis et al. 2024). Consequently, the model includes more degrees of freedom than the previous approach. Since the stiffeners are assigned independent kinematic fields, their deformations are not constrained by the shell, allowing them to experience local buckling (Poorveis et al. 2024). This makes the second discrete approach the most comprehensive modeling technique for stiffened shells, as it can capture both global and local buckling phenomena. For instance,′ Kabir (2006) developed a finite strip model of shell stiffened by stringers and used discrete approach to investigate the buckling behavior of stringer-stiffened shell.

On other hand, a review of the literature shows that different techniques such as nonlinear geometry analysis, advanced approach based on Koiter's theory, and eigenvalue analysis have been used to determine the buckling load of cylindrical shells (Barbero et al. 2017; Wang et al. 2018). While eigenvalue buckling analysis is a simplified linear method that does not account for imperfections or nonlinear effects, Koiter's theory is suitable for the fast evaluation of geometrical imperfections on the buckling behavior of shell structures (Barbero et al. 2017). However, eigenvalue buckling analysis remains a valuable tool for performing extensive parametric studies during the early design phase. Its exceptionally low computational cost enables rapid comparative assessments of how different geometric and material parameters affect buckling behavior. In the eigenvalue method, firstly a pre-buckling analysis is performed to obtain the initial displacements and rotations of the shell under external loading in order to derive the geometric stiffness matrix of the structure (Taig, Ranzi, and Luongo 2016). In fact, the geometric stiffness matrix of the structure significantly depends on the stress distribution in the shell obtained in the pre-buckling analysis step (Pi and Bradford 2010; Hancock and Pham 2017; Pezeshky and Mohareb 2018). Several studies have been performed on effect of displacements and stress obtained from pre-buckling analysis step on the buckling load of different types of structures obtained from eigenvalue analysis. For instance, Clark and Knoll (1958) investigated influence of displacement obtained from pre-buckling analysis on the lateral buckling of beam-column. Wang et al. (1992) developed an approach to investigate the effect of pre-buckling stress distribution on the elastic buckling of rectangular plate under membrane stress. Wang et al. (1992) showed that pre-buckling stress distribution significantly changes the buckling behavior of plate with thickness-to-span ratio.

Alternatively, recent research has shown that non-uniform loading conditions can affect the buckling load of shell structures. Ramachandra, Dey, and Kumar (2022) conducted a comprehensive theoretical and numerical investigation on the stability of plates and shell panels subjected to nonuniform in-plane loading, highlighting that these loading distributions generate asymmetric fields of stress, which can markedly reduce buckling loads as compared to uniform loading conditions. Jiao et al. (2023) considered thin-walled cylindrical shells that were subjected to localized axial compression and demonstrated that sensitivity to initial imperfection is significantly increased under such conditions, resulting in an increased degradation of buckling strength. In a somewhat similar study, Azzuni and Guzey (2018) used local perturbation theory as a method to demonstrate that nonuniform external loading, even on simpler circular ring models, can modify both the pre-buckling deformation modes and corresponding post-buckling paths, ultimately threatening structural stability. In the context of composite plates, Kumar, Lal, and Sutaria (2023) investigated buckling behavior of laminated structures with different hole geometries under uniform and nonuniform mechanical and thermal loadings. It is shown from their findings that nonuniform loading not only alters the location of critical stress concentrations but also amplifies the effect of geometric discontinuities. Together, the experiments highlight the vital importance of accommodating realistic, nonuniform stress conditions in both analytical analysis and design procedures to enable proper buckling performance predictions and sound structural design integrity.

A review of literature reveals that although stress distribution of pre-buckling has a significant effect on the buckling load of structure, the effect of stress distribution of pre-buckling on the buckling load of stringer-stiffened elliptical composite cylindrical shell is not investigated in the previous studies. This research was carried out to eliminate this limitation. In fact, the novelty of this study stands for the investigation of stress distribution and stringer slenderness effects on the axial buckling of stringer stiffened composite elliptical shell under different external loading patterns through implementation of the advanced discrete modeling strategy that allows independent displacement of stringers, thereby enabling the capture of stringer local buckling effects. While it is true that buckling analysis of stiffened composite cylindrical shells has been extensively investigated in previous research, this study introduces a novel combination of several key aspects that

have not been simultaneously addressed in the literature which are including: (1) buckling of stringer stiffened composite elliptical shell, (2) utilizing advanced discrete approach for simulating stiffened shell and considering local buckling of stringers, (3) assessment interaction between pre-buckling stress distribution and stringer slenderness, and (4) considering three physically motivated and distinctly distributed pre-buckling stress fields reflect realistic loading conditions. In this regard, the stringer-stiffened elliptical composite cylindrical shell was simulated using FSM and three types of pre-buckling stress distribution (reflecting three distinct realistic loading conditions) were considered in the model. Through a parametric study, the buckling load of stiffened composite cylindrical shells with varied geometric characteristics of the stiffeners, altering the slenderness of the stiffeners, has been examined under varying distributions of pre-buckling stresses.

## 2. Development of finite strip model

In order to develop the finite strip model of a composite cylindrical shell that has been stiffened with stringers and determine the axial buckling load of the shell under axial compression, a FORTRAN environment code has been created. The FSM was used to model a stringer-stiffened elliptical cylindrical shell with length L and thickness h, as shown in Fig. 1. Figure 1(a) illustrates the 3D geometry and the local tangential-normal coordinate system (x, $\theta$, and z), while Fig. 1(b) shows the 2D cross-sectional properties, including the major and minor radii (a and b), shell thickness h, stiffener spacing $b_e$, and stiffener dimensions $h_s$ as the stiffener thickness and $d_s$ as the stiffener depth. Stringer-stiffened shell is divided into multiple strip elements along the longitudinal axis of the cylinder, as illustrated in Fig. 2. Each strip includes two nodal lines, and five degrees of freedom u, v, w, $\varphi_x$, and $\varphi_\theta$ are considered at each node. The symbols u, v, and w indicate displacements in the x, $\theta$, and z directions, correspondingly. Furthermore, $\varphi_x$ and $\varphi_\theta$ represent rotations about x and $\theta$, respectively.

The displacement and rotation of strip elements were estimated in this work using Lagrangian and harmonic shape functions in both longitudinal and circumferential directions. In order to satisfy the shell's simply supported boundary conditions, the longitudinal Sine and Cosine harmonic functions were taken into consideration. Additionally, circumferentially directed two-nodded Lagrangian functions were employed. Equation (1) was used to determine the displacement and rotation of the strip element based on first order shear deformation theory (Poorveis et al. 2019).

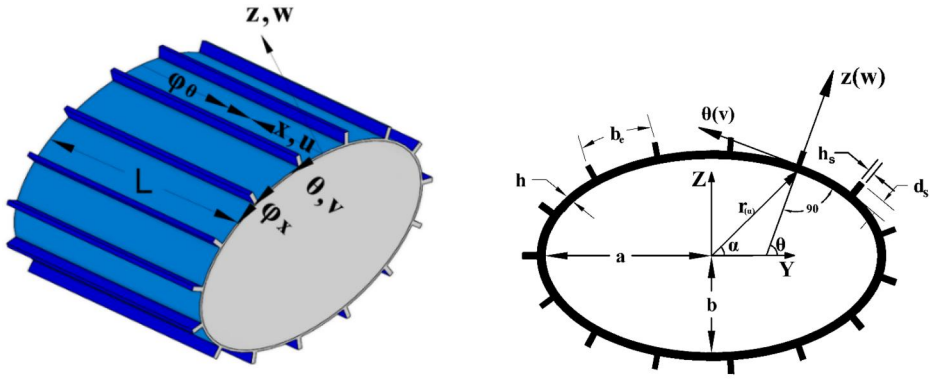


Figure 1. Simulation of a stringer-stiffened cylindrical shell (a) geometry, (b) cross-section.

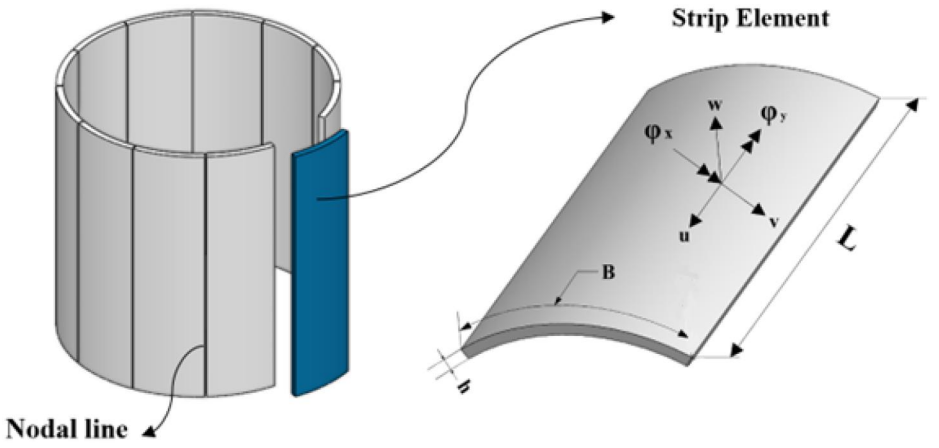


**Figure 2.** Discretized cylindrical shell and strip element.

$$\begin{Bmatrix} u \\ v \\ w \\ \varphi_x \\ \varphi_\theta \end{Bmatrix} = \begin{Bmatrix} \sum_{r=1}^{M}\sum_{s=1}^{N} u_{rs}.\cos(a_r x).N_s(\eta) + \sum_{s=1}^{N} u_{0s}.N_s(\eta).\left(\frac{1}{2}-\frac{x}{L}\right) \\ \sum_{r=1}^{M}\sum_{s=1}^{N} v_{rs}.\sin(\alpha_r.x).N_s(\eta) \\ \sum_{r=1}^{M}\sum_{s=1}^{N} w_{rs}.\sin(\alpha_r.x).N_s(\eta) \\ \sum_{r=1}^{M}\sum_{s=1}^{N} \varphi_{xrs}.\cos(\alpha_r.x).N_s(\eta) \\ \sum_{r=1}^{M}\sum_{s=1}^{N} \varphi_{\theta rs}.\sin(\alpha_r.x).N_s(\eta) \end{Bmatrix} \quad (1)$$

In Eq. (1), s is the number of nodes, $M$ represents the total number of harmonics, $N$ is the total number of nodes taken into consideration for each strip element, and $r$ stands for harmonic number. $\alpha_r$ equals $\frac{m\pi}{L}$. Additionally, the axial displacement coefficient is $u_{s0}$. Furthermore, for the s-th node and r-th harmonic, the unknown coefficients of displacement/rotation of the strip element are $u_{rs}, v_{rs}, w_{rs}, \varphi_{xrs}$, and $\varphi_{\theta rs}$. In Eq. (1), $N_s$ stands for Lagrangian shape function of s-th node and is obtained using Eq. (2) by Khajehdezfuly, Poorveis, and Nazarinia (2023).

$$N_1(\eta) = \frac{1-\eta}{2}$$
$$N_2(\eta) = \frac{1+\eta}{2} \quad (2)$$

The local coordinate, denoted by $\eta$ in Eq. (2), ranges from $-1$ to 1. $\eta$ is related to tangential coordinate ($\theta$) through a linear relationship. The displacements and rotations were estimated using a linear combination of Lagrangian shape functions Eq. (3).

$$f(\eta) = \sum_{j=1}^{n} \alpha_j N_j(\eta). \quad (3)$$

The unknown coefficient of the $j$th node is represented by $\alpha_j$ in Eq. (3), where $n$ equals 2. This study allows for the estimation and investigation of the local buckling of the shell and

stringer since the displacements and rotations are defined individually for the stringers and shell. This work began by determining the displacement and rotation of the shell placed on top of the mid-plane. Equation (4) (Reddy 2006) was then utilized to determine the displacement and rotation of all other planes, excluding the mid-plane.

$$\begin{Bmatrix} \bar{\varepsilon}_{xx} \\ \bar{\varepsilon}_{\theta\theta} \\ \bar{\gamma}_{x\theta} \end{Bmatrix} = \begin{Bmatrix} \varepsilon_{xx} \\ \varepsilon_{\theta\theta} \\ \gamma_{x\theta} \end{Bmatrix} + z \begin{Bmatrix} k_{xx} \\ k_{\theta\theta} \\ k_{x\theta} \end{Bmatrix}. \tag{4}$$

The distance in the thickness direction of the shell between the mid-plane and any arbitrary plane is denoted by z in Eq. (4). The mid-plane normal strain in x direction is denoted by $\varepsilon_{xx}$, the mid-plane normal strain in $\theta$ direction by $\varepsilon_{\theta\theta}$, the x$\theta$ plane shear strain is denoted by $\gamma_{x\theta}$, the bending curvature in x direction is represented by $k_{xx}$, the bending curvature in $\theta$ direction by $k_{\theta\theta}$, and the torsional curvature in the x$\theta$ plane is represented by $k_{x\theta}$. Furthermore, $\bar{\varepsilon}_{xx}, \bar{\varepsilon}_{\theta\theta,}$ and $\bar{\gamma}_{x\theta}$ are the equivalent strains of an arbitrary plane that is situated z away from the shell's mid-plane (in the thickness direction). This study included both linear and nonlinear strain–displacement equations for the shell's mid-plane. These relations were obtained from earlier analysis conducted by Khayat, Poorveis, and Moradi (2016), which relied on first shear deformation theory and simplified Sander's theory Eqs. (5) and (6).

$$\begin{Bmatrix} \varepsilon_{xx} \\ \varepsilon_{\theta\theta} \\ \gamma_{x\theta} \\ \gamma_{xz} \\ \gamma_{\theta z} \\ k_{xx} \\ k_{\theta\theta} \\ k_{x\theta} \end{Bmatrix} = \begin{Bmatrix} \dfrac{\partial u}{\partial x} \\ \dfrac{\partial v}{r\partial\theta} + \dfrac{w}{r} \\ \dfrac{\partial v}{\partial x} + \dfrac{\partial u}{r\partial\theta} \\ \varphi_x + \dfrac{\partial w}{\partial x} \\ \varphi_\theta + \dfrac{\partial w}{r\partial\theta} - \dfrac{v}{r(\theta)} \\ \dfrac{\partial \varphi_x}{\partial x} \\ \dfrac{\partial \varphi_\theta}{r\partial\theta} \\ \dfrac{\partial \varphi_\theta}{\partial x} + \dfrac{\partial \varphi_x}{r(\theta)\partial\theta} \end{Bmatrix} \tag{5}$$

The shear linear strain in the thickness direction of the xz plane is represented by $\gamma_{xz}$ in Eq. (5), while the shear linear strain in the thickness direction of the $\theta$z plane is represented by $\gamma_{\theta z}$. The other linear strains have already been defined. Radius of curvature at $\theta$ coordinate is also represented as r($\theta$). As nonlinear terms of strains (Jiao et al. 2023), $\varepsilon_{xx}^{nL}$, $\varepsilon_{\theta\theta}^{nL}$ and $\gamma_{x\theta}^{nL}$, appear in Eq. (6).

$$\begin{Bmatrix} \varepsilon_{xx}^{nL} \\ \varepsilon_{\theta\theta}^{nL} \\ \gamma_{x\theta}^{nL} \end{Bmatrix} = \begin{Bmatrix} \dfrac{1}{2}\left(\dfrac{\partial w}{\partial x}\right)^2 \\ \dfrac{1}{2r^2}\left(\dfrac{\partial w}{\partial \theta}\right)^2 + \dfrac{1}{2}\left(\dfrac{v^2}{r^2} - \dfrac{2v\partial w}{r^2\partial\theta}\right) \\ \dfrac{1}{r}\left(\dfrac{\partial w}{\partial x} \cdot \dfrac{\partial w}{\partial \theta}\right) - \left(\dfrac{v}{r} \cdot \dfrac{\partial \omega}{\partial x}\right) \end{Bmatrix} \tag{6}$$

Equation (7) by Khayat, Poorveis, and Moradi (2017) can be used to generate the generalized stress vector ($\{\sigma\}$) for any arbitrary point on the shell's mid-plane.

$$\sigma^T = \{N_{xx}, N_{\theta\theta}, N_{x\theta}, M_{xx}, M_{\theta\theta}, M_{x\theta}, Q_{xz}, Q_{\theta z}\} \tag{7}$$

The membrane resultant force in x direction is denoted by $N_{xx}$ in Eq. (7), the membrane resultant force in $\theta$ direction is denoted by $N_{\theta\theta}$, and the resultant shear force per unit length of the plane perpendicular to thickness direction is represented by $N_{x\theta}$. Additionally, the bending moment per unit length about $\theta$ axis is represented by $M_{xx}$, the bending moment per unit length in the x$\theta$ plane by $M_{x\theta}$, and the shear forces per unit length in thickness direction are shown by $Q_{xz}$ and $Q_{\theta z}$. Equation (8) was utilized to get the generalized stress-strain relationship, as reported by Khayat, Poorveis, and Moradi (2017).

$$\begin{Bmatrix} N_{xx} \\ N_{\theta\theta} \\ N_{x\theta} \\ M_{xx} \\ M_{\theta\theta} \\ M_{x\theta} \\ Q_{xz} \\ Q_{\theta z} \end{Bmatrix} = \begin{bmatrix} [A] & [B] & 0 \\ [B] & [D] & 0 \\ 0 & 0 & [A_s] \end{bmatrix} \begin{Bmatrix} \varepsilon_{xx} \\ \varepsilon_{\theta\theta} \\ \gamma_{x\theta} \\ k_{xx} \\ k_{\theta\theta} \\ k_{x\theta} \\ \gamma_{xz} \\ \gamma_{\theta z} \end{Bmatrix} \tag{8}$$

Equation (9) is used to generate all of the elements of the material matrices ([A], [B], and [D]) that are displayed in Eq. (8).

$$\begin{aligned} A_{ij} &= \sum_{k=1}^{n} \left[\bar{Q}_{ij}\right]_k (h_k - h_{k-1}) \;\; i,j = 1,2,6, \\ A_s &= k_s \sum_{k=1}^{n} \left[\bar{Q}_{ij}\right]_k (h_k - h_{k-1}) \;\; i,j = 4,5 \\ B_{ij} &= \frac{1}{2} \sum_{k=1}^{n} \left[\bar{Q}_{ij}\right]_k \left({h_k}^2 - {h^2}_{k-1}\right) \;\; i,j = 1,2,6 \\ D_{ij} &= \frac{1}{3} \sum_{k=1}^{n} \left[\bar{Q}_{ij}\right]_k \left({h_k}^3 - {h^3}_{k-1}\right) \;\; i,j = 1,2,6 \end{aligned} \tag{9}$$

In Eq. (9), $A_{ij}$, $B_{ij,}$ and $D_{ij}$ stands for axial, axial-bending, and bending stiffness, respectively. Moreover, $K_s$ is shear correction factor and considered as 5/6. In Eq. (9), $k_s$ represents the shear correction factor, which is taken as 5.6 in this study. Additionally, $h_k$ and $h_{k-1}$ denote the distances of the upper and lower surfaces of layer K of the composite from the midplane of the shell. In Eq. (10), the matrix $[\bar{Q}]$ represents the reduced stiffness matrix generalized to global coordinates. The generalization of the components of this matrix is based on Reddy's study. The components of the matrix [Q] in local coordinates are calculated according to Eq. (10).

$$\begin{Bmatrix} Q_{11} \\ Q_{12} \\ Q_{22} \\ Q_{66} \\ Q_{44} \\ Q_{55} \end{Bmatrix} = \begin{Bmatrix} \dfrac{E_{11}}{1 - \nu_{12}\nu_{21}} \\ \dfrac{\nu_{21}E_{11}}{1 - \nu_{12}\nu_{21}} \\ \dfrac{E_{22}}{1 - \nu_{12}\nu_{21}} \\ G_{12} \\ G_{23} \\ G_{13} \end{Bmatrix} \tag{10}$$

The modulus of elasticity (E) and Poisson's ratio (v) of material are respective values in Eq. (10). In order to get the elastic stiffness matrix of the strip element $[K_E]$, the virtual internal work ($\delta W_{int}^{L}$) was written in the form of Eq. (11) done by linear virtual strains (Eq. 4) and their associated generalized stresses (Eq. 7) by Moradi, Poorveis, and Khajehdezfuly (2022).

$$\delta W_{int}^{L} = \int_{x}\int_{\theta}\left(N_{xx}\delta\varepsilon_{xx}{}^{l} + N_{\theta\theta}\delta\varepsilon_{\theta\theta}{}^{l} + N_{x\theta}\delta\gamma_{x\theta}{}^{l} + M_{xx}\delta k_{xx} + M_{\theta\theta}\delta k_{\theta\theta} + M_{x\theta}\delta k_{x\theta} + Q_{xz}\delta\gamma_{xz} + Q_{\theta z}\delta\gamma_{\theta z}\right) r d\theta dx \tag{11}$$

The linear virtual strains in Eq. (11) are represented by $\delta$X. It should be noted that the r tends to infinity and turns into a plane strip to obtain the elastic stiffness matrix of the stringer. Both the shell and the stringer have the identical displacements and rotations at their common nodes. In fact, stringer and shell were tied to each other in this study.

In order to investigate the influence of different pre-buckling stress distributions in stringer-stiffened cylindrical shells, three distinct types of axial compressive loading were applied to the model. Each loading scenario corresponds to a specific boundary condition and induces a characteristic mechanical response in the structure. The first loading condition applies a uniformly distributed axial pressure solely to the ge of the shell, with the stringers remaining unaffected by any external load. This configuration, commonly adopted in earlier studies, is referred to in this work as the conventional loading pattern (CLP). A schematic illustration of this case is shown in Fig. 3(a), while Fig. 4 presents a sectional view of the cylindrical shell subjected to this loading

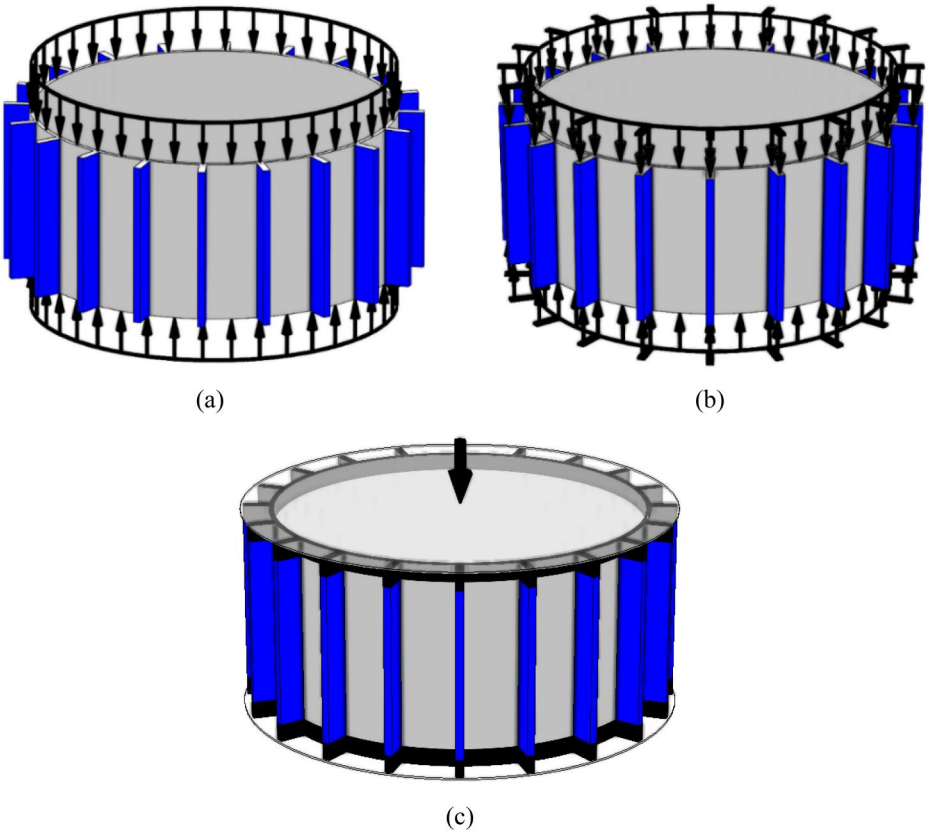


**Figure 3.** 3D model of applied loading patterns (a) conventional loading pattern (CLP), (b) axial pressure on edges of shell and stringer (PSS), (c) applying same displacement on edges of shell and stringer (ASD).

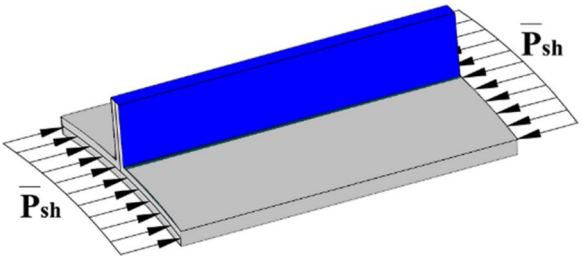


**Figure 4.** Conventional loading pattern (CLP).

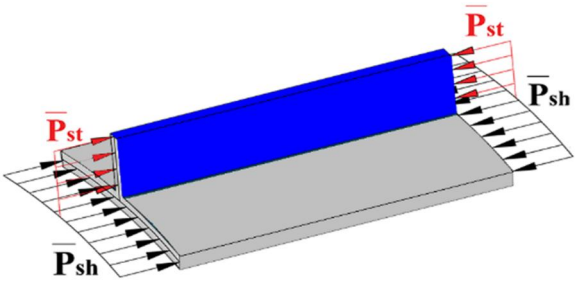


**Figure 5.** Axial pressure on edges of shell and stringer (PSS).

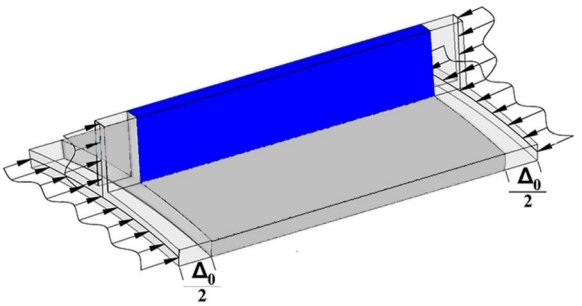


**Figure 6.** Applying same displacement on edges of shell and stringer (ASD).

condition. In the second loading condition, a uniformly distributed axial pressure is applied simultaneously to the edges of both the shell and the stringers. The total axial force is divided between the shell and stringers in proportion to their respective cross-sectional areas. This case is referred to as axial Pressure on edges of shell and stringer (PSS). The corresponding schematic is shown in Fig. 3(b), and Fig. 5 provides a sectional view of the cylinder under this loading. The third loading condition involves applying equal axial displacements to the outer edges of both the shell and stringers, without the direct application of external pressure. This scenario, referred to as Applying Same Displacement on edges of shell and stringer (ASD), produces a load distribution based on the relative axial stiffness of the components. Displacement compatibility between the shell and stringer edges is enforced using the penalty approach. This configuration is illustrated in Fig. 3(c), and the associated sectional view is shown in Fig. 6.

A review of the characteristics of three loading patterns considered in this study (CLP, PSS, and ASD) enrich the understanding of difference between them. In the CLP loading case, the axial compressive force is applied exclusively to the edge surface of the cylindrical shell, without directly engaging the stringers. Accordingly, this loading scenario closely replicates practical situations where, due to manufacturing constraints or geometric configurations, the shell length

marginally exceeds the length of the stringers. Even a slight mismatch can prevent load transfer to the stringers, making CLP a reliable representation of real-world applications in which the stringers are indirectly loaded. On other hand, the PSS loading condition assumes that the applied load is uniformly distributed across both the shell and stringer edge surfaces in proportion to their respective areas. While this assumption is useful for theoretical and comparative purposes, particularly to assess how load sharing affects buckling behavior, it does not realistically reflect how loads are transferred in practice. Differences in boundary conditions, material properties, and laminate stacking sequences often prevent such idealized distribution, making PSS more suitable for academic evaluation than for structural design. The ASD loading case introduces a more physically realistic approach by allocating the applied load between the shell and the stringers based on their axial stiffness. This approach inherently considers the influence of material properties and geometric stiffness, and thus better captures actual load paths under complex boundary and support conditions. Among the three loading scenarios, ASD is the most accurate representation of real-life load transfer mechanisms, especially when stringers are fully engaged. The mathematical formulations for CLP and PSS loading patterns are provided in Appendix A and also, Appendix B includes the mathematical formulations for ASD loading pattern.

Only the pre-buckling analysis incorporated the changes made to the stiffness and load vector in the third loading case. The eigenvalue buckling analysis carried out in this loading case is identical to the first and second loading instances taken into account in this research. Equation (12) was utilized to determine the geometric stiffness matrix of the strip element ($K_G$) by utilizing the nonlinear internal virtual work of pre-buckling membrane forces ($N^0_{xx}$, $N^0_{\theta\theta}$, and $N^0_{x\theta}$).

$$\delta W^{NL}_{int} = \int_x \int_\theta \left( N^0_{xx}\delta\varepsilon^{nl}_{xx} + N^0_{\theta\theta}\delta\varepsilon^{nl}_{\theta\theta} + N^0_{x\theta}\delta\gamma^{nl}_{x\theta} \right) r d\theta dx \tag{12}$$

In Eq. (12), $\delta\varepsilon^{nl}_{xx}$, $\delta\varepsilon^{nl}_{\theta\theta}$ and $\delta\varepsilon^{nl}_{x\theta}$ represent the nonlinear virtual strains corresponding to $\varepsilon^{nL}_{xx}$, $\varepsilon^{nL}_{\theta\theta}$, and $\gamma^{nL}_{x\theta}$, respectively. Equation (12) was generalized and simplified to derive geometrical stiffness matrix (Kumar, Lal, and Sutaria 2023). The components of the geometric stiffness matrix ($K_G$) rely on the model's rotation and displacement since the geometric stiffness matrix ($K_G$) depends on nonlinear strains. In fact, in order to obtain the geometrical stiffness matrix of the strip element, the model's displacement and rotation are required. A pre-buckling analysis was carried out in this study. To achieve the geometrical stiffness matrix for every loading case presented in the previous section, a unique axial pressure was applied on the stiffened shell. It should be mentioned that the $r$ parameter in the geometrical stiffness matrix of the strip element was taken into account as a large number (tends to infinity) in order to calculate the geometrical stiffness matrix of the stringer. The model's geometrical stiffness matrix was developed by assembling the geometrical stiffness matrices of the strip and stringer elements.

The eigenvalue problem was taken into consideration in order to determine the axial buckling load of the model (Eq. 13) (Ramachandra, Dey, and Kumar 2022). In Eq. (13), $K_E$ is the model's elastic stiffness matrix, $K_G$ is its geometrical stiffness matrix, $\lambda$ is the eigenvalue, and $\varphi$ is the model's mode shape. Sub-space solution algorithm was used to solve the eigenvalue problem in this study (Hancock and Pham 2017).

$$(K_E - \lambda.K_G)\varphi = 0 \tag{13}$$

## 3. Model validation

The validity of the results obtained from the model developed in this study was evaluated in two phases. In the first phase, the results were compared with data available in the literature. In the second phase, a comparison was conducted between the results obtained from the FSM model

developed in this study and those obtained from a finite element method (FEM) model implemented in ABAQUS software. The details of both validation phases are provided below.

### 3.1. First phase

In this phase, a comparison was made between the results obtained from the model and those of the literature. Kabir (2006) investigated static buckling behavior of composite cylindrical shells reinforced by longitudinal stiffeners, using geometric nonlinear analysis. In their study, the kinematic relationship of the shells was grounded in Donnell's nonlinear theory, and first-order shear deformation was applied to both the shell and the stiffeners. In their study, longitudinal stiffeners were attached to the cylindrical shell as discrete element under axial pressure. They represented displacements, rotations, and mutual forces in terms of Fourier series expansions as independent approximate solution functions, and nonlinear equilibrium equations were derived using the Ritz method.

Figure 7 illustrates the configuration of the longitudinal stiffener placed on the shell considered in Kabir and Poorvies's research. The stiffened shell considered in Kabir and Poorveis's research was modeled in this study. In Table 1, the geometric specifications of the modeled shell in the study by Kabir and Poorveis 2006) are provided. The buckling loads obtained from the model developed in this study and that presented in Kabir and Poorveis 's research are provided in Table 2. As presented in this table, the difference between the buckling loads is about 2% which

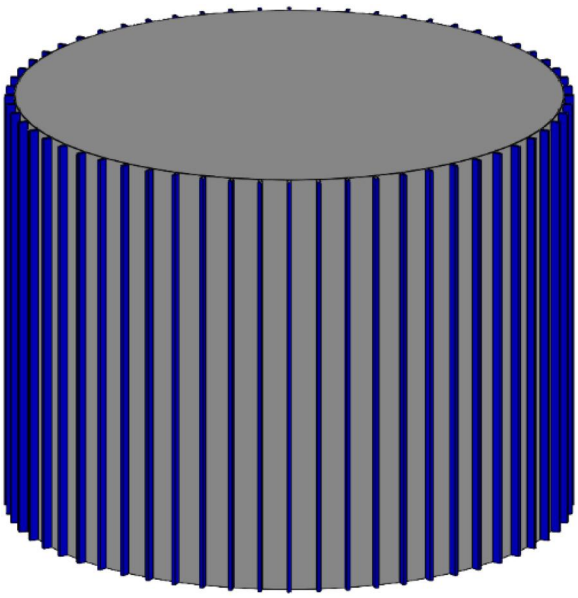

**Figure 7.** Isotropic shell stiffened by 60 stringers simulated by Kabir and Poorveis (2006).

**Table 1.** Specifications of cylindrical shell with 60 stiffeners.

| E(kg/mm$^2$) | $\upsilon$ | L(mm) | R(mm) | h(mm) | nst | ds(mm) | t(mm) |
|---|---|---|---|---|---|---|---|
| 7500 | 0.3 | 965.2 | 242.57 | 0.719 | 60 | 7.6645 | 2.4484 |

**Table 2.** Comparison of buckling load (kg/mm): this study vs. literature.

| This study | (Kabir and Poorveis 2006) | Percentage of Error |
|---|---|---|
| 20.98 | 21.45 | 2.19% |

is negligible. It shows that the model developed in this study is capable to calculate the buckling load of the stiffened cylindrical shells.

### 3.2. Second phase

To further assess the validity of the developed model, a comparative analysis was conducted between the results obtained from the proposed model and those derived from a finite element model developed using ABAQUS software. The meshed model developed in ABAQUS is shown in Fig. 8. The model consists of a cylindrical structure with a constant radius of 100 mm and three different lengths: 100, 200, and 400 mm, as illustrated in subfigures 8(a), 8(b), and 8(c), respectively.

The material was assumed to be isotropic, with Young's modulus of 2000 MPa and Poisson's ratio of 0.3. The upper and lower edges of the cylinder were constrained in all directions except the longitudinal axis, allowing movement only in the axial direction. An axial compression load was applied to the shell edges. These conditions were used consistently in both models (FEM and FSM) to enable direct comparison of the resulting buckling loads.

Table 3 presents the results obtained from FSM and FEM models. As observed, the discrepancy between the results remains within an acceptable range, with a maximum difference of approximately 4.58% for shell length of 400. The minimal variation (0.14%) at shell length of 100 confirms the robustness and consistency of the developed FSM model in predicting the buckling loads across a range of shell geometries.

## 4. Results and discussion

A parametric study was carried out to investigate the effects of different parameters including number of stringers, depth of stringers, stringer area index, b/a (major to minor axes ratio), composite layup and length of shell on the buckling load and pre-buckling stress in cylindrical shell. Stringer area index is the ratio of the cross-sectional area of the reinforcement to the cross-sectional area of the shell shown in Eq. (14).

$$\text{Stringer area index} = \frac{\text{Total cross} - \text{sectional stringer area}}{\text{Total cross} - \text{sectional shell area}}. \tag{14}$$

Table 4 presents the values considered for each parameter. The properties of each composite layer are presented in Table 5. As presented in Table 4, six different four-ply laminates were considered in this study: $[45, 0, 90, -45]$, $[45, -45]_2$, $[45, 90, -45, 90]$, $[90, 0]_s$, $[90, 0]_2$ and $[45, 0, -45, 0]$.

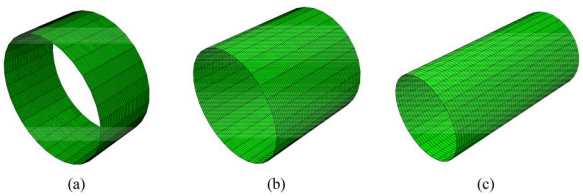


**Figure 8.** 3D buckling mode shapes of cylindrical shell with different lengths obtained from ABAQUS (a) $L = 100$, (b) $L = 200$, (c) $L = 400$.

**Table 3.** Comparison of buckling loads obtained from FSM and FEM models.

| Length (mm) | ABAQUS: FEM (N/mm) | FORTRAN: FSM (N/mm) | Difference (%) |
|---|---|---|---|
| 100 | 11.926 | 11.909 | 0.14% |
| 200 | 11.434 | 11.750 | 2.76% |
| 400 | 11.074 | 11.606 | 4.58% |

**Table 4.** Parameters and their values considered in parametric study.

| Parameter | | Values |
|---|---|---|
| Number of stringers | | 20, 30, 40 |
| Depth of stringers (mm) | | 3, 5, 7, 9 |
| Stringer area index (%) | | 5, 10, 15, 20, 25, 30 |
| Minor to major radius ratio | | 0.4, 0.5, 0.6, 0.7, 0.8, 0.9, 1.0 |
| Length of shell (mm) | | 50, 100, 150, 200 |
| Composite layup | 4 layers | $[45, 0, 90, -45]$, $[45, -45]_2$, $[45, 90, -45, 90]$, $[90, 0]_s$, $[90, 0]_2$, $[45, 0, -45, 0]$ |
| | 6 layers | $[90, 0]_3$, $[90, 0, 90]_s$, $[45, -45]_3$ |
| | 8 layers | $[90, 0]_4$, $[90, 0]_{2s}$, $[45, -45]_4$ |

**Table 5.** Properties of each composite layer considered for shell and stringers.

| Property | Value |
|---|---|
| $E_{11}$ | 206.844 GPa |
| $E_{22}$ | 18.615 GPa |
| $G_{12}$ | 4.48162 GPa |
| $G_{13}$ | 4.48162 GPa |
| $G_{23}$ | 2.55107 GPa |
| $\nu$ | 0.21 |

These stacking sequences were deliberately selected to provide a representative comparison between quasi-isotropic, cross-ply, angle-ply, and mixed laminates, while systematically varying symmetry and balance, two key factors known to control laminate stiffness and coupling behavior. For example, the symmetric cross-ply $[90, 0]_s$ eliminates bending-extension coupling, whereas its antisymmetric counterpart $[90, 0]_2$ includes bending-membrane coupling stiffness. The antisymmetric balanced angle-ply $[45, -45]_2$ introduces bending–twisting coupling but suppresses in-plane extensional-shear coupling, while the mixed layups provide insight into the combined effects of axial and shear-oriented plies. This set of laminates therefore enables a systematic evaluation of how stacking sequence affects stiffness, anisotropy, and coupling responses, consistent with laminate design principles reported in the literature. Building on this framework, six- and eight-ply laminates were also considered to assess the influence of number of plies at constant overall thickness. The $[90, 0]_3$ and $[90, 0]_4$ layups extend the cross-ply family, allowing evaluation of how increasing ply count while refining ply thickness influences load transfer and structural response. The symmetric sequences $[90, 0, 90]_s$ and $[90, 0]_2$ highlight the role of laminate symmetry in suppressing undesirable coupling effects and promoting balanced stiffness distributions at higher number of layers. Meanwhile, the angle-ply laminates $[45, -45]_3$ and $[45, -45]_4$ were selected to test whether increasing number of plies alters the shear-dominated behavior typical of $\pm 45$ laminates, or if their response remains largely governed by in-plane shear characteristics. Together, the chosen 4-, 6-, and 8-ply laminates provide a coherent and representative set that systematically addresses the effects of ply orientation, symmetry, and number of layers on the buckling behavior of composite shells (Jones 2018; Ogunleye et al. 2022; Patel, Sonkar, and Patel 2025).

Shell boundary conditions were defined in accordance with NASA SP-8007 (NASA, 1968), which provides correction factors for axial buckling loads based on end constraints such as simply supported and clamped conditions. Composite lay-up compressive properties were determined using data derived from ASTM D6641 (ASTM International 2016), ensuring consistency with standardized testing protocols for laminate stiffness and strength. The results obtained from the parametric study are provided in the following sub-sections.

### 4.1. Stringer depth

Figure 9 illustrates the influence of varying the stringer area index on the buckling load of cylindrical shells reinforced with stiffeners of different depths, specifically for shells containing 20

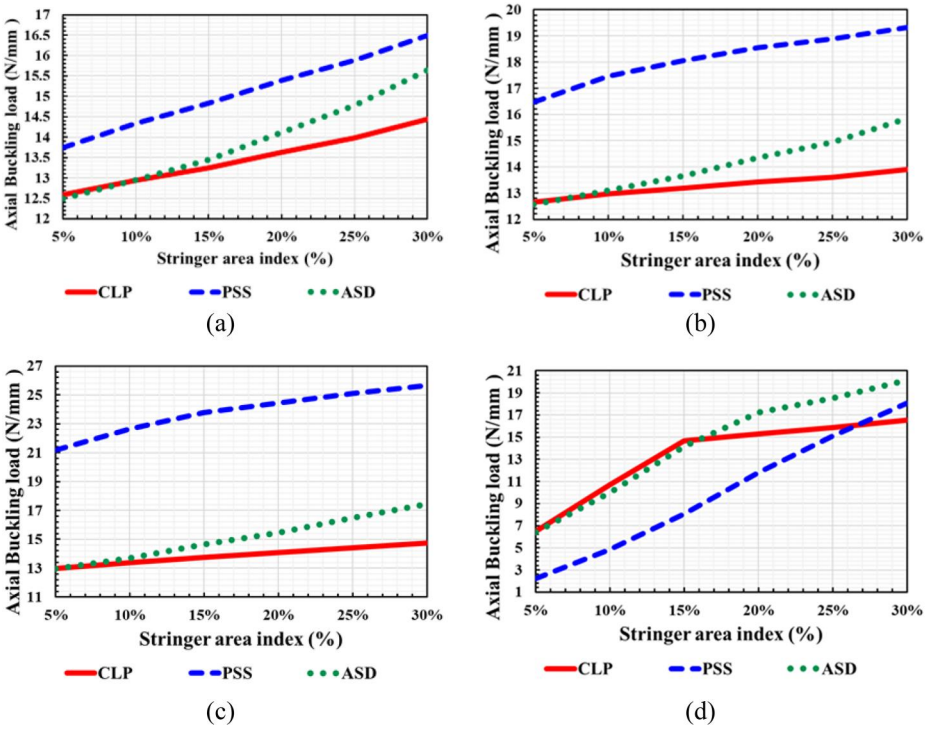


**Figure 9.** Axial buckling load of cylindrical shell with 40 stiffeners and different stiffener depths under various loading patterns (a) stiffener depth 3, (b) stiffener depth 5, (c) stiffener depth 7, (d) stiffener depth 9.

stiffeners. The graphs show that, for a constant stiffener depth and number of stringers, increasing the stringer area index (which corresponds to a thicker stiffener) results in a higher buckling load of the shells. When comparing the buckling loads under different loading patterns, an examination of Fig. 9(a) through 9(d), corresponding respectively to stringer depths of 3, 5, 7, and 9, reveals distinct trends. Under the CLP loading condition, an increase in stringer depth initially causes a decrease in buckling load. However, this downward trend reverses sharply at a stringer depth of 9, where significant local buckling of the stringers occurs, causing a substantial reduction in buckling load by approximately 20–50%. In this study, local buckling is defined as deformation occurring specifically within the stringers, whereas general buckling refers to the overall structural instability of the shell. It is important to note that under the CLP loading condition, local buckling emerges due to the stress distribution transferred from the shell to the stringers.

An analysis of the buckling load variations with increasing stringer depth under ASD loading, as illustrated in Fig. 9(a) through 9(d) (corresponding respectively to stringer depths of 3, 5, 7, and 9), reveals distinct behaviors based on the stringer area index. For shells with a low stringer area index (5–15%), the buckling load decreases by approximately 8–50% as the stringer depth increases, indicating increased susceptibility of slender stringers to both local and general buckling. In contrast, shells with a higher stringer area index (20–30%) exhibit an increase in buckling load ranging from 15% to 30% with greater stringer depth, reflecting the beneficial effect of thicker stiffeners in enhancing shell stability. Local buckling under ASD loading is influenced not only by the stress transferred from the shell to the stringers but also by the additional stresses induced in the stringers due to the imposed axial displacement on their edges.

An analysis of the buckling load variations with increasing stringer depth under the PSS loading condition reveals distinct trends. As shown in Fig. 9(a–d), across all stringer area indices,

show that an initial increase in stringer depth up to 7 results in a substantial rise in the buckling load (reaching approximately 50%). However, beyond this depth, further increase of stinger depth leads to a decline in buckling load. Notably, at a stringer depth of 9, shells with a low stringer area index (5% and 10%) exhibit a significant reduction in buckling load, approximately 80%, which is attributed to severe local buckling of the stringers. In contrast, shells with a higher stringer area index (30%) experience only a slight decrease in buckling load compared to lower area index cases at the same depth.

This pronounced local buckling behavior under the PSS loading condition results from the combined stresses applied directly to the stringer edges and those transferred from the shell edges. This interaction is reflected in the buckling load trends, as shown in Fig. 9(c) and 9(d), where the buckling load under PSS is lower than that under CLP at higher stringer depths.

In Fig. 10, two Elements have been chosen as samples to assess the pre-buckling stress of cylindrical shells. These sections consist of the stiffener element along the radius of the circle entitled as (b) and the associated shell element entitled as (a).

Figure 11 provides insight into the distribution of longitudinal pre-buckling stresses in specific elements of the shell and stringer. The graphs in Fig. 11 are divided such that Fig. 11(a), 11(c), 11(e), and 11(g) correspond to shell elements, while Fig. 11(b), 11(d), 11(f), and 11(h) relate to stringer elements, both of which are depicted in Fig. 9. In the case of CLP loading, an increase in the depth of stringers leads to an increase in pre-buckling stress on the shell, as there is no external load on the stringers. Conversely, under ASD loading, the pre-buckling stress in the shell section shows minimal change with varying stringer's depth. These trends are illustrated in Fig. 11(a), 11(c), 11(e), and 11(g), where the CLP and ASD loading conditions are shown as legends in the graphs. However, an increase in stringer depth corresponds to a decrease in pre-buckling stress in the stringers, akin to the observations in CLP loading, as clearly illustrated in Fig. 11(b), 11(d), 11(f), and 11(h), which show a progressive reduction in pre-buckling stress values with increasing depth. Within the PSS loading scenario, a comparison of the shell element graphs (Fig. 11a, 11c, 11e, and 11g) and stringer element graphs (Fig. 11b, 11d, 11f, and 11h), as indicated by the PSS legends, reveals that pre-buckling stress in the shell elements increases with rising stringer depth, whereas pre-buckling stress in the stringer elements decreases as depth increases. This loading scenario reveals that in shells with shallower stringers, stress accumulation is more pronounced in the middle longitudinal sections of the shell. In contrast, stringers with

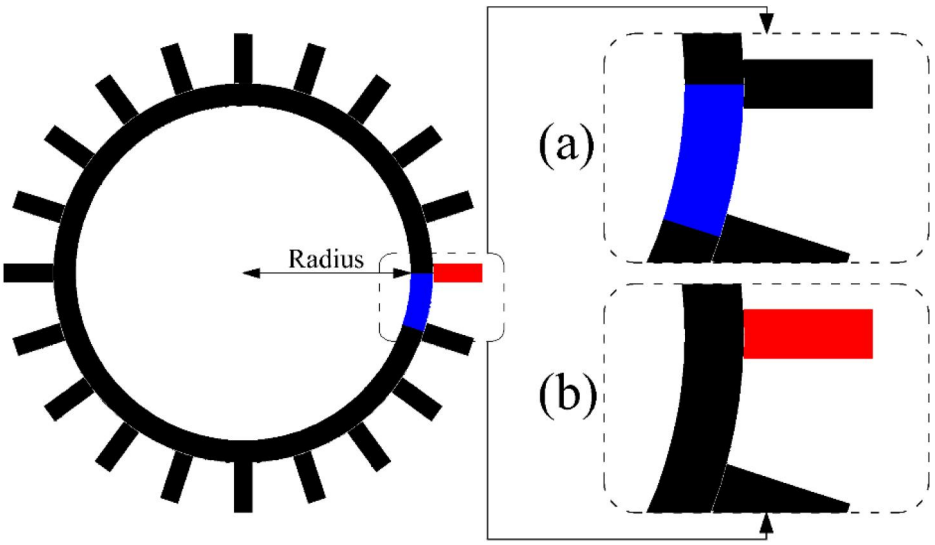


**Figure 10.** Shell and stringer elements taken into account for pre-buckling analysis of oval cross section.

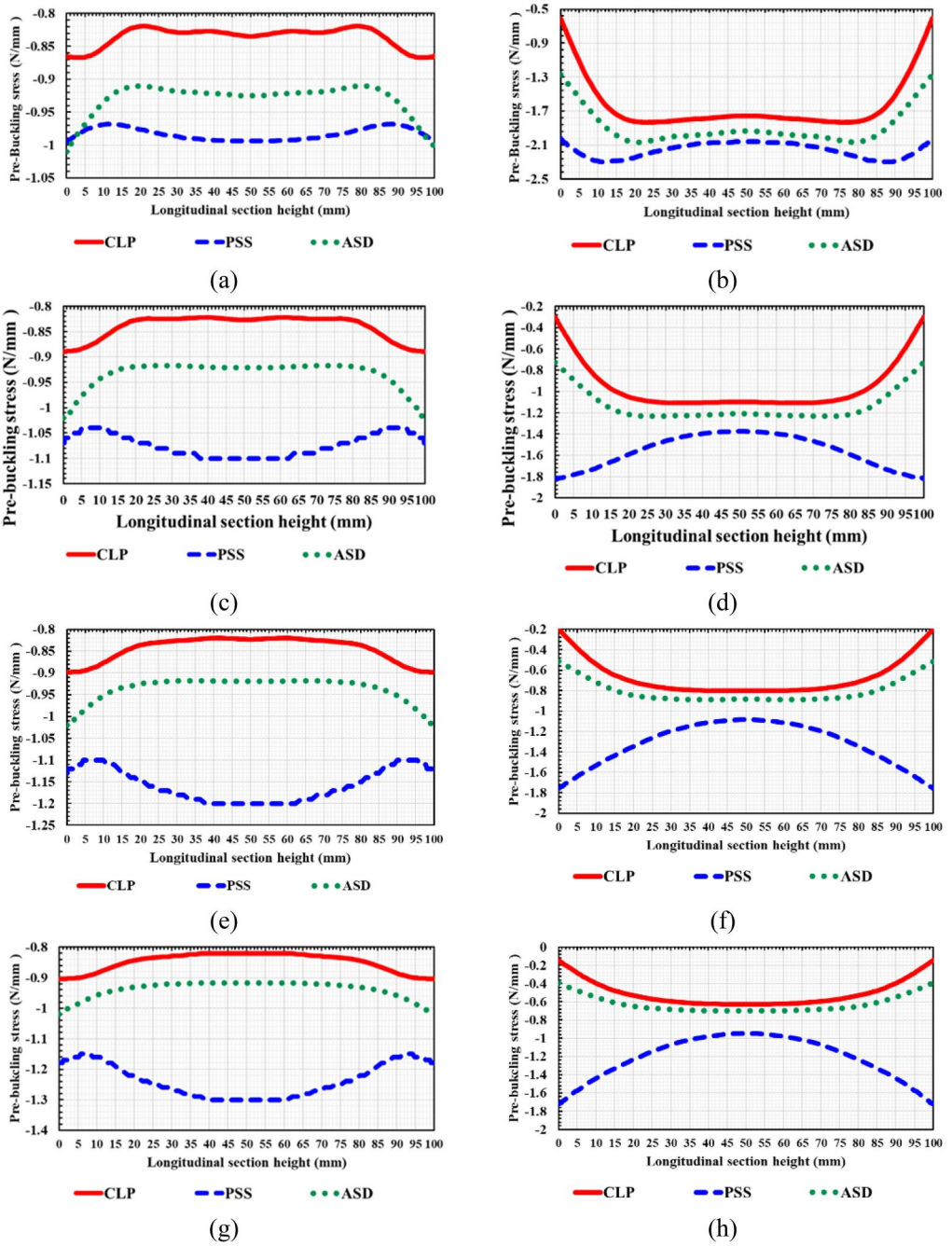


**Figure 11.** longitudinal pre-buckling stress distribution in shell and stiffener elements for a shell stiffened by 20% stringer area index (a) Shell element – Stiffener depth 3, (b) Stiffener element – Stiffener depth 3, (c) Shell element - Stiffener depth 5, (d) Stiffener element - Stiffener depth 5, (e) Shell element – Stiffener depth 7, (f) Stiffener element – Stiffener depth 7, (g) Shell element – Stiffener depth 9, (h) Stiffener element – Stiffener depth 9.

greater depth (9 mm) as illustrated in Fig. 11(h) exhibit higher pre-buckling stress accumulation in the upper longitudinal sections of the stiffeners, consequently contributing to the onset of local buckling in the stringers. To provide a clearer understanding of pre-buckling stress distribution and the structural behavior of cylindrical shells, a three-dimensional visualization of stress

patterns on the shell and stringer surfaces has been generated and is presented in Fig. (12). Specifically, subfigures 12(a), 12(d), 12(g), and 12(j) correspond to the CLP loading condition; 12(b), 12(e), 12(h), and 12(k) represent the PSS loading condition; and 12(c), 12(f), 12(i), and 12(l) depict the ASD loading condition – each set reflecting increasing stringer depths of 3, 5, 7, and 9 mm, respectively.

As illustrated in all Fig. 12 subfigures corresponding to the CLP loading condition (12(a), 12(d), 12(g), and 12(j)), the stress exhibits higher magnitudes in the upper longitudinal level of the shell, gradually decreasing in the middle levels. This difference becomes a bit more noticeable as the stringers get deeper, In the PSS loading condition, for stringers with a depth of 3 mm, as shown in Fig. 12(b), the stress initially increases and then decreases along the longitudinal direction. As the stringer depth increases, this stress distribution pattern changes, while in the shell element, stresses remain relatively constant with minimal variation along the shell length.

In contrast, the stringer element with a depth of 3 mm, as shown in Fig. 11(b), exhibits variations in stress along its length. As the stringer depth (observed in the subsequent subplots of

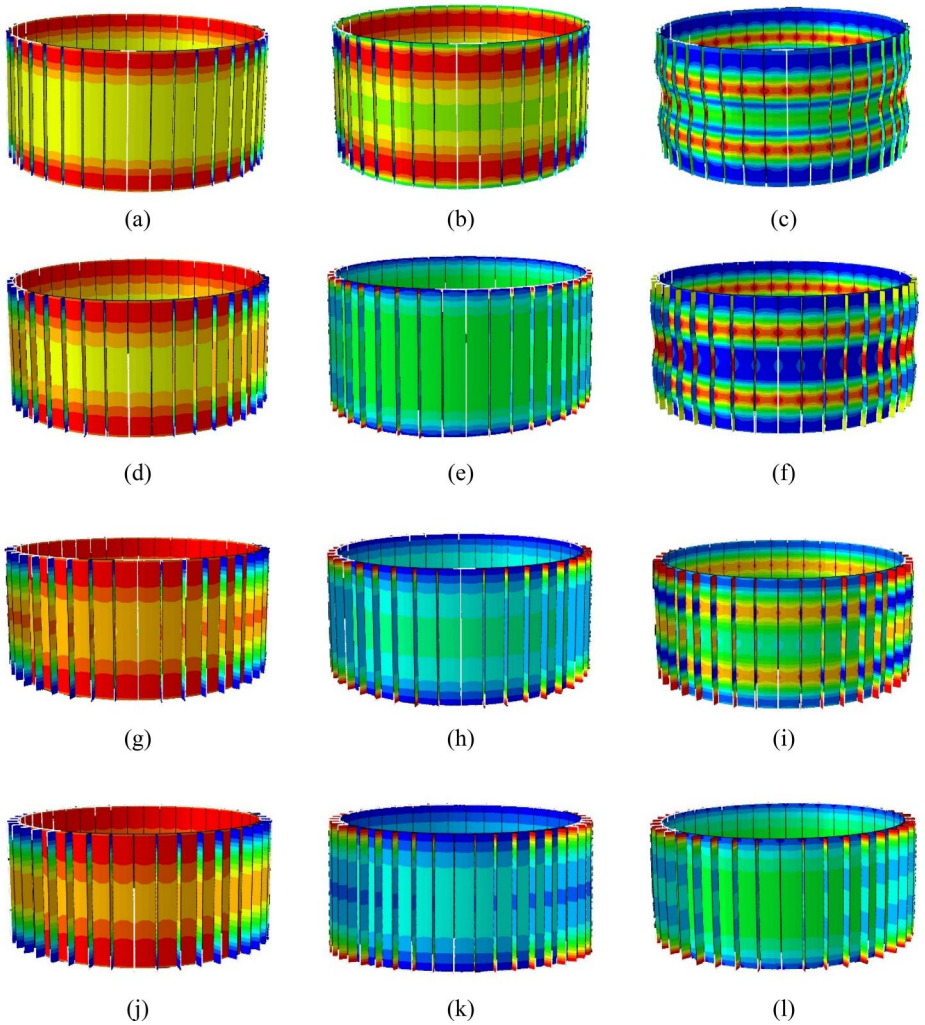


**Figure 12.** 3D representation of stress distribution in shells featuring various stringer depths with 20% stringer area index under diverse loading patterns (a) CLP – stiffener depth 3, (b) PSS – stiffener depth 3, (c) ASD – stiffener depth 3, (d) CLP – stiffener depth 5, (e) PSS – stiffener depth 5, (f) ASD – stiffener depth 5, (g) CLP – stiffener depth 7, (h) PSS – stiffener depth 7, (i) ASD – stiffener depth 7, (j) CLP – stiffener depth 9, (k) PSS – stiffener depth 9, (l) ASD – stiffener depth 9.

Fig. 12 corresponding to the PSS loading condition.) the slenderness ratio rises, causing greater stress build-up in the upper longitudinal sections of the stringers, followed by a gradual decrease in stress further along the stringer. This stress concentration leads to local buckling and increased structural vulnerability. Comparing with ASD loading, the applied displacement is evident in the shell. Stress values in the shell element display an irregular trend along longitudinal direction, initially decreasing and then increasing. Notably, the shell with a stringer depth of 9 mm, as illustrated in Fig. 12(l), exhibits significant stress concentrations at the upper regions of the stringers. This localized stress concentration facilitates the onset of local buckling in shells exhibiting lower stringer area indices and elevated slenderness ratios. It is important to emphasize that while pre-buckling stress analysis provides valuable insight into shell behavior under various loading conditions, the most comprehensive and accurate results were obtained through eigenvalue analysis.

To enhance the understanding of failure mechanisms associated with local and general buckling, Fig. (13) presents six mode shapes for cylindrical shells with stringers at stringer area indices of 5% and 30%, and a stringer depth of 9, subjected to three different loading conditions. As illustrated, the cylinder with a stringer area index of 5% and stringer depth of 9 exhibits local buckling under all loading types. In the PSS and ASD loading scenarios (illustrated in Fig. 13b and 13c), the local buckling initiates at the stringers due to localized stress concentrations where the load is applied near the upper and lower longitudinal sections. In contrast, under CLP loading as shown in Fig. 13(a), the local buckling of the stringer predominantly occurs in the mid-longitudinal section, where stress is transferred from the shell to the stringers. When examining the cases with a 30% stringer area index, no local buckling is observed. However, there are notable weaknesses in the stringer regions due to the excessive depth, rendering them more susceptible to deformation. In these cases, the maximum displacement caused by buckling occurs primarily in the shell sections, particularly in the upper and lower longitudinal regions of the shell, consistent with the observations in Fig. 13(d–f).

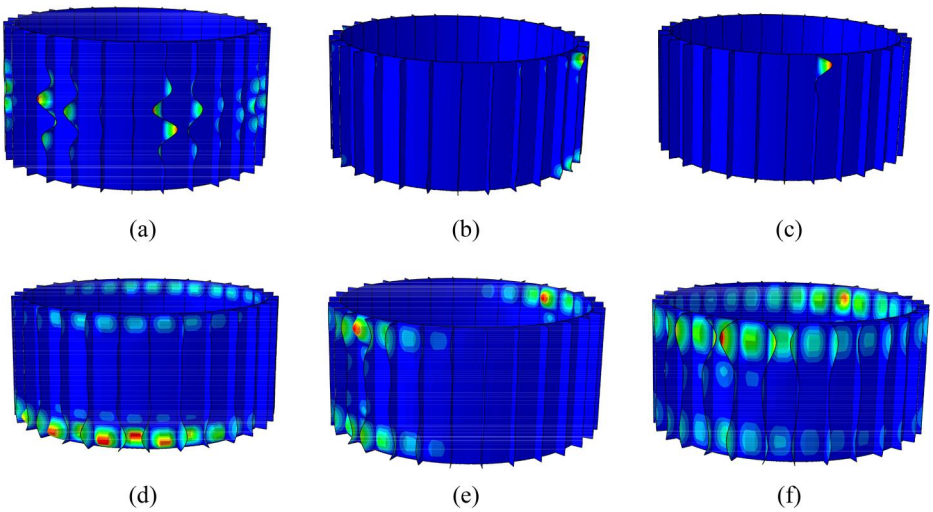


**Figure 13.** Buckling mode shapes of stiffened cylindrical shells under CLP, PSS, and ASD loading conditions by considering stringer depth of 9 and for stringer area indices of 5% and 30%. (a) CLP – 5% stringer area index, (b) PSS – 5% stringer area index, (c) ASD – 5% stringer area index, (d) CLP – 30% stringer area index, (e) PSS – 30% stringer area index, (f) ASD – 30% stringer area index.

### 4.2. Number of stringers

Figure 14 presents the buckling behavior of cylindrical shells with 20, 30, and 40 stringers, each with a stringer depth of 9 mm. Under the CLP loading condition, local buckling is observed at a 5% stringer area index for the shell with 30 stringers (Fig. 14b), and at both 5% and 10% for the shell with 40 stringers (Fig. 14c). This trend indicates an increasing susceptibility to local buckling with a higher number of stringers.

For the ASD loading condition, local buckling is not present in the shell with 20 stringers (Fig. 14a). However, it becomes more apparent in configurations with a greater number of stringers, as seen by comparing the ASD results across the subfigures. In some cases, the buckling load under ASD is lower than that under CLP, primarily due to early local buckling in the stringers. This comparison is evident by examining the CLP and ASD legends in each subplot.

Under PSS loading, increasing the number of stringers further reduces resistance to local buckling. In particular, the shell with 40 stringers (Fig. 14c) shows local buckling at nearly all stringer area indices except 30%. This observation is supported by comparing the PSS curves across all subfigures, highlighting the weakening effect of thinner, more numerous stringers under this loading scenario.

In Fig. 15, the pre-buckling stress distribution is illustrated for a shell featuring 20% stringer area index with varying quantities of 20, 30, and 40 stringer numbers, all with a depth of 9 mm. A visual representation of pre-buckling stresses (shown in Fig. 15a, 15c, and 15e for the shell elements and Fig. 15(b), 15(d), and 15(f) for the stringer elements) in the longitudinal sections of both the shell and the stringers are evaluated to reach a deep understanding of effect of external loading pattern on the stress distribution.

In the case of the shell subjected to CLP loading, it is evident that in the section of the shell with 20% stringer area index, the highest pre-buckling stress occurs at higher longitudinal

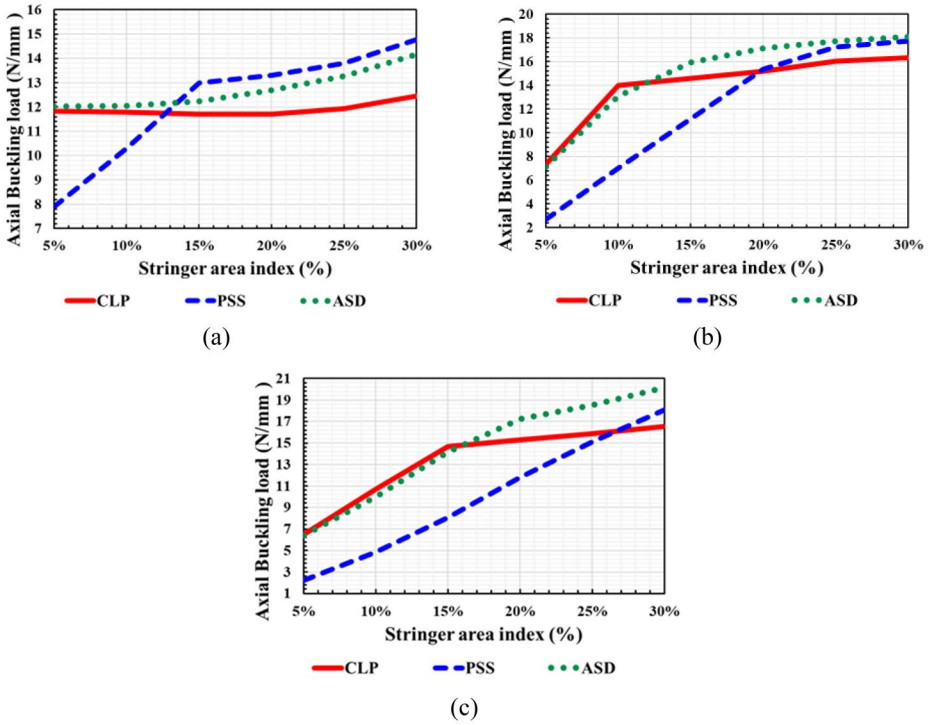


Figure 14. Axial buckling load of cylindrical shell with 9 mm stiffener depth and stiffened by different number of stiffeners (a) 20 stiffeners, (b) 30 stiffeners, (c) 40 stiffeners.

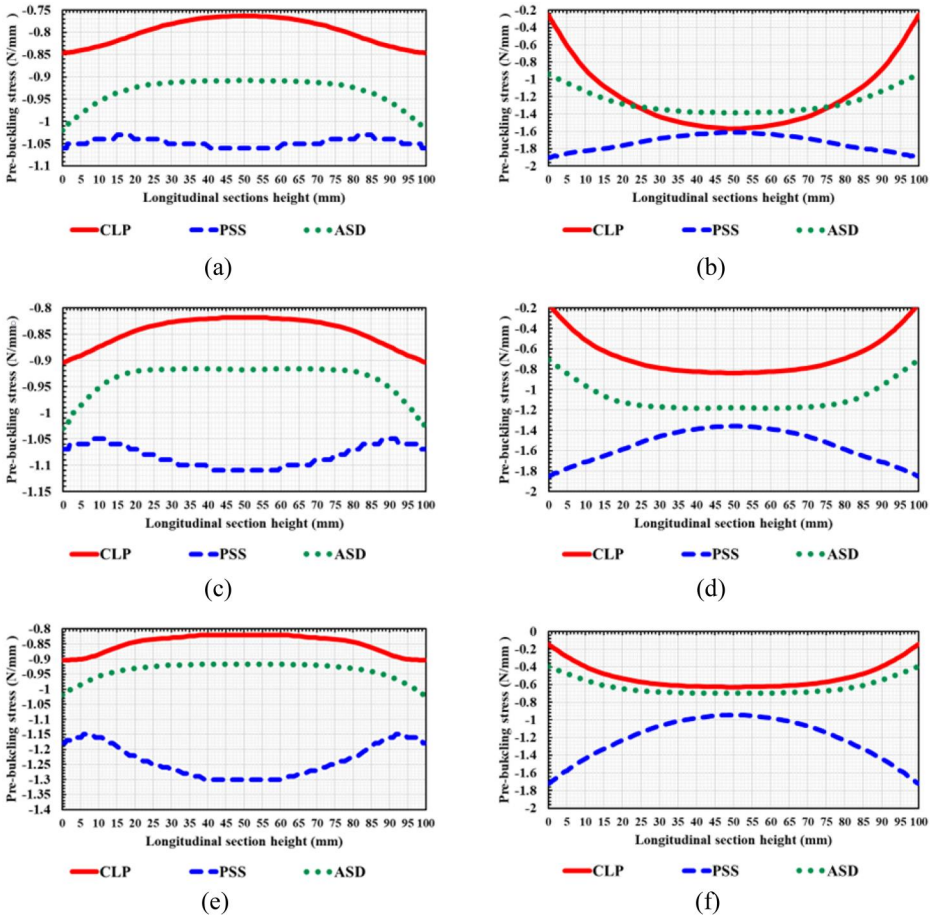


**Figure 15.** Longitudinal pre-buckling stress distribution on shell and stiffener elements in a shell stiffened by 20% stringer area index, stiffener depth of 9 mm and different number of stiffeners (a) shell element – 20 stiffeners, (b) stringer element – 20 stiffeners, (c) shell element – 30 stiffeners, (d) stringer element – 30 stiffeners, (e) shell element – 40 stiffeners, (f) stringer element – 40 stiffeners.

sections of the shell element plots, which correspond to Fig. 15(a), 15(c), and 15(e). Conversely, in the highest longitudinal sections of stringers, the stress attains its lowest value. The maximum pre-buckling stress in the longitudinal sections of the stringers is at middle longitudinal levels of the stringers, as illustrated in the stringer element plots shown in Fig. 15(b), 15(d), and 15(f). As the number of stringers increases, a noticeable increase in pre-buckling stress is observed within the shell elements, as evident from the comparison between Fig. 15(a) and 15(e). In contrast, the stringer elements – shown in Figs. 15(b) and 15(f) – exhibit a more regular stress distribution with increasing stringer quantity, characterized by elevated pre-buckling stresses in the upper longitudinal sections and a corresponding decrease in stress at intermediate longitudinal levels. This behavior is observed in the shell under ASD loading, mirroring the performance of the shell under CLP loading. It is notable that, with an increase in the number of stringers, the difference in these stresses between the longitudinal sections of the shell and the stringer diminish. This reduction is attributed to the enhanced regularization of stress distribution across the shells. Under PSS loading, a distinct pattern is observed where pre-buckling stresses increase notably in the shell elements, especially within the middle longitudinal sections. In the stringer elements, an increase in the number of stringers corresponds to a reduction in pre-buckling stress at the middle longitudinal levels. Specifically, after the number of stringers increases, the stress

difference between the middle and upper longitudinal sections of the stringer element reaches approximately 60%, as shown in Fig. 15(f). It is noteworthy that based on the stresses observed in the shell and stringer under different loading cases, a conclusion can be drawn that higher external loading on stringer elements results in higher pre-buckling stress in stringers particularly in the upper longitudinal levels of the stringer sections.

### 4.3. Stringer area index

This section presents an evaluation of the pre-buckling stress distribution in shells with varying stringer area indices subjected to different loading conditions. Figure 16 provides a comparative analysis of shells with 40 stringers at two stringer area indices: 5% (the minimum), illustrated in Fig. 16(a) and 16(b) for shell and stringer elements, respectively, and 30% (the maximum), depicted in Fig. 16(c) and 16(d) for shell and stringer elements respectively. Figure (16), It is evident that, with an increase in the stringer area index, the stress distribution pattern in shells under different loading conditions becomes more consistent. Specifically, the pre-buckling stress within the shell's longitudinal sections decreases, while the stress carried by the stringers increases, indicating a greater share of load being transferred to the stiffer stringers. Additionally, the increase in the thickness of the stringers results in higher stress values in the central sections of the stringers. To gain a more comprehensive understanding of the influence of the stringer area index on the distribution of pre-buckling stresses, the influence of stringer area index on the pre-buckling stresses of a cylindrical shell featuring 40 stringers with a depth of 5 was investigated and the obtained results are shown in Fig. 17. which comprises nine subfigures illustrating pre-buckling stress distributions across different stringer area indices and loading conditions. Specifically, Fig. 17(a), 17(d), and 17(g) corresponds to CLP loading with stringer area indices of 10%, 20%, and 30%, respectively. Similarly, Fig. 17(b), 17(e), and 17(h) represent ASD loading under the same respective area indices, while Fig. 17(c), 17(f), and 17(i) displays the results for PSS loading at these increasing stringer area index levels.

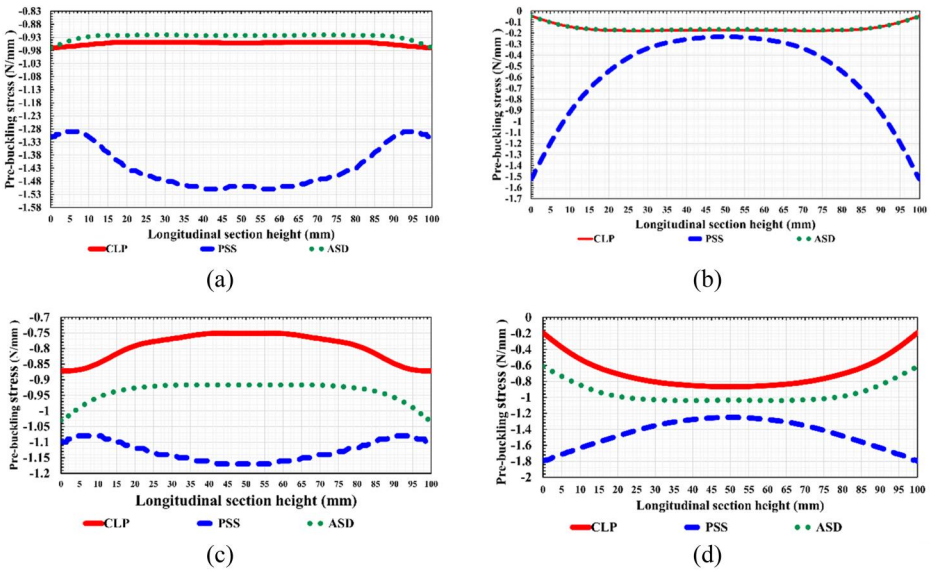


**Figure 16.** stress distribution on shell and stiffener elements in a shell stiffened by 40 stringers with depth of 9 mm and considering different stringer area indices (a) shell element – 5% stringer area index, (b) stringer element – 5% stringer area index, (c) shell element – 30% stringer area index, (d) stringer element – 30% stringer area index.

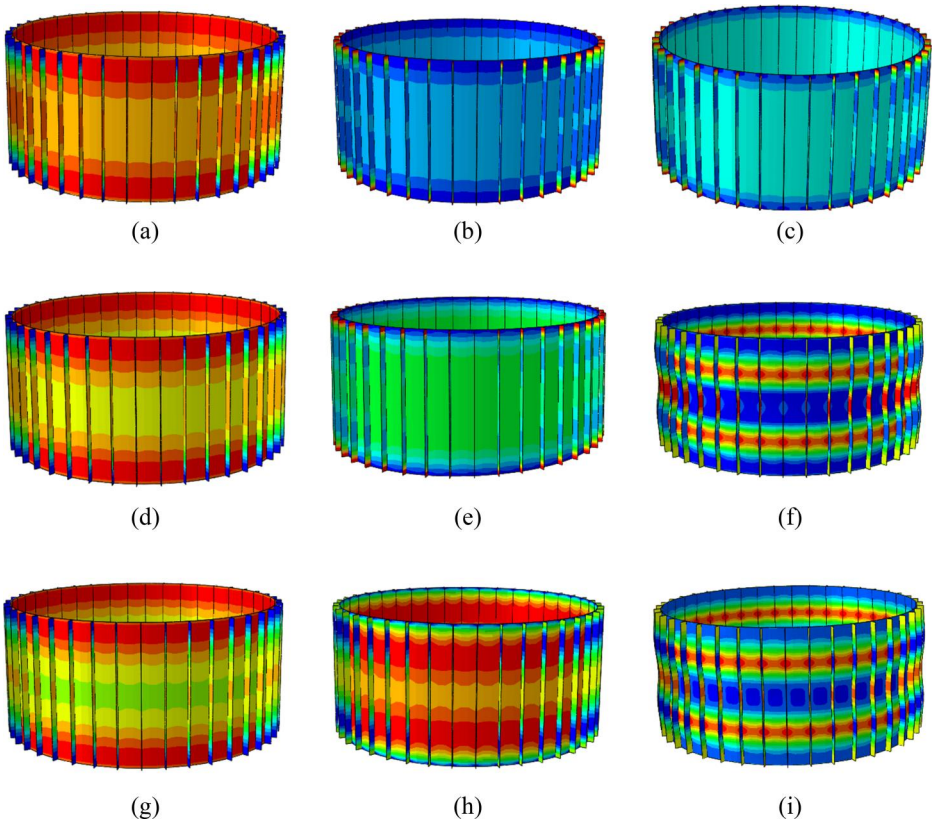


**Figure 17.** 3D representation of stress distribution in shells featuring different stringer area indices with 9 mm stringer depth under various loading patterns (a) 10% – CLP, (b) 10% – PSS, (c) 10% – ASD, (d) 20% – CLP, (e) 20% – PSS, (f) 20% – ASD, (g) 30% – CLP, (h) 30% – PSS, (i) 30% – ASD.

Under CLP loading, it is evident that the increase of stringer area index correlates with decrease of pre-buckling stress in the upper longitudinal levels of the shell and increase in pre-buckling stresses in longitudinal stringer sections. Subsequently, under PSS loading, at lower stringer area index values, localized buckling manifests at upper levels of stringers, resulting by thinner longitudinal stringers. However, as the stringer area index increases, a notable shift occurs, stress tolerance in the stringer elements increases, leading to a decrease in the probability of local buckling in the stringers. Lastly, under ASD loading, analogous to PSS loading, the shell featuring 10% stringer area index (Fig. 17c) exhibits local buckling of the stringers. Notably, with an increase in the stringer area index (Fig. 17g and 17i), stress reduction is visibly in upper longitudinal level of stringer sections.

### *4.4. Shell length*

In Fig. 18, the influence of the length of the cylindrical shell (slenderness ratio of shell section) on the buckling load is explored for a shell stiffened with 30 stringers having a depth of 5.

The observation reveals that an increase in the shell length corresponds to a decrease in the buckling load. This trend holds true for both CLP and ASD loading cases across all shell lengths. However, when assessing the buckling behavior against PSS loading case, it is apparent that applying a portion of external load on the edges of the stringers leads to local buckling. This is particularly evident when the shell is stiffened with stringer area index of 5% at lengths of 50 and 100 illustrated in Fig. 18(a) and 18(b). To delve deeper into this issue, the distribution of

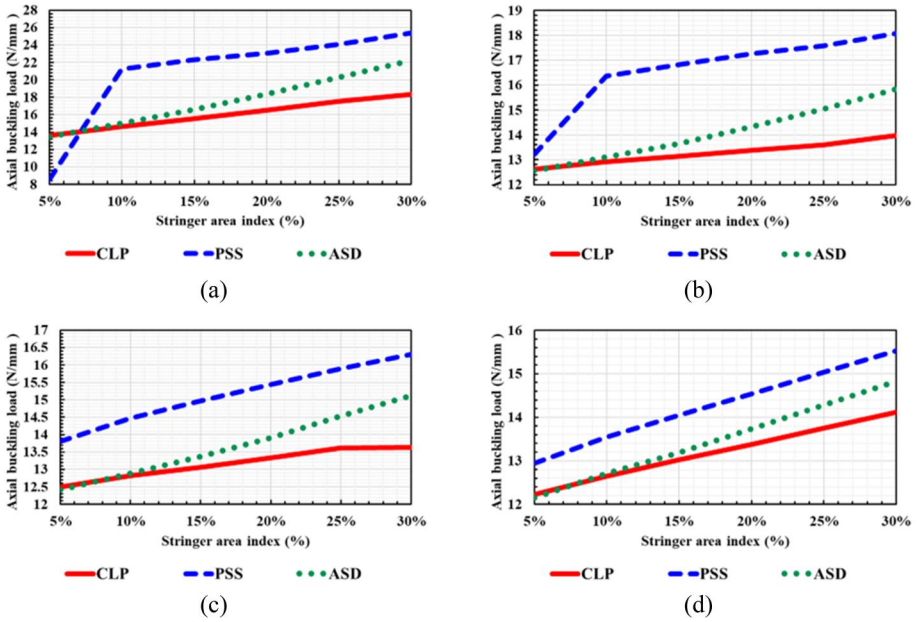


**Figure 18.** Effect of length of cylinder on axial buckling load of cylindrical shell stiffened by 30 stiffeners with depth of 5 (a) length 50, (b) length 100, (c) length 150, (d) length 200.

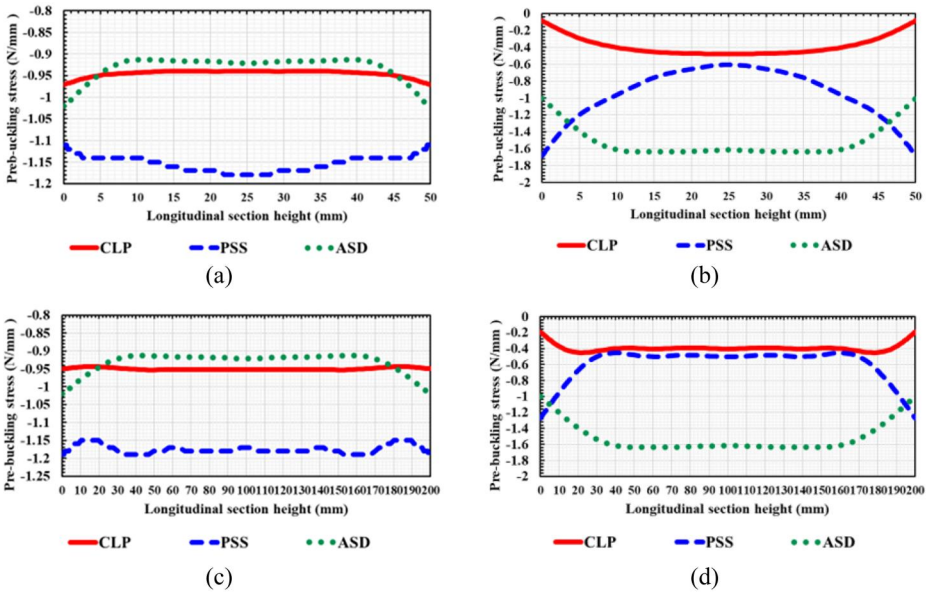


**Figure 19.** Effect of cylinder length on longitudinal pre-buckling stress distribution in shell and stringer elements obtained for a shell stiffened by 30 stiffeners with depth of 5 and stiffener area index of 5% (a) shell section – length of 50, (b) stiffener section – length of 50, (c) shell section – length of 200, (d) stiffener section – length of 200.

pre-buckling stresses in the longitudinal direction of the shell and stringers for the shell reinforced with 30 stringers, featuring a depth of 5, and a stringer area index of 5% was derived and is shown in Fig. 19.

Figure 19 reveals that as the shell length increases, the distribution of pre-buckling stress under CLP and ASD loading cases remains relatively stable, both in the shell and stringers. A marginal

uptick in stress is noticeable in the stringers, accompanied by a slight decrease in the shell. However, an examination of the buckling behavior under PSS loading case demonstrates a distinctive trend. The increase of length of the structure under this specified pattern increases pre-buckling stress within the longitudinal sections of the shell due to the applied load. This trend can be seen by comparing the results presented in Fig. 19(a) and 19(c). Conversely, there is a simultaneous decrease in pre-buckling stress within the longitudinal sections of the stiffeners, The increase in structural length effectively reduces the likelihood of local buckling, particularly in configurations with a low stringer area index (5–10%). This can be seen while examining Fig. 20(b) and 20(d), where the longitudinal pre-buckling stress distribution shows lower stress concentrations in the upper and lower sections, accompanied by a more uniform stress distribution across the middle sections of the structure.

### 4.5. Shell cross-section

In order to assess the influence of the b/a parameter on shells with varied geometrical characteristics, models were constructed for shells with 30 stiffeners and stiffener depth of 5. These models encompassed reinforcement level indices of 10%, 20%, and 30%, and were subjected to three distinct loading patterns. The effect of b/a (ratio of the small radius to the large radius of the oval section) on buckling load of the shell was investigated and shown in Table 6.

It can be seen that the change in the cross-sectional shape of the shell and its change from circle to oval has led to the reduction of buckling load under different loading cases. As presented in Table 6, buckling load has decreased by about 50% in oval-shaped shells with a ratio of $b/a = 0.4$. As b/a increases, the buckling load has become closer to the shell in the circular state. Cylindrical shells with oval cross-sections respond similarly to those with circular cross-sections under various loading conditions. Specifically, when the stringer area index increases, the

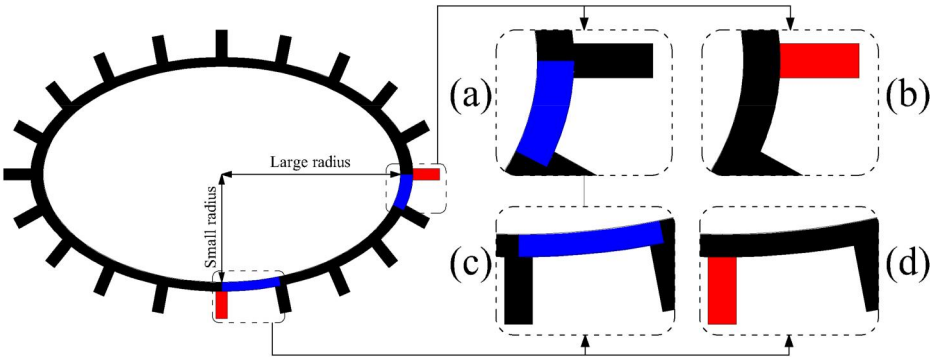


**Figure 20.** Shell and stringer sections taken into account for pre-buckling analysis of oval cross section.

**Table 6.** Buckling load of cylindrical shell with 30 stiffeners (depth of 5) and different b/a ratios (N/mm).

| Stiffener characteristics | | Loading | b/a | | | | | | |
|---|---|---|---|---|---|---|---|---|---|
| N | % | Pattern | 0.4 | 0.5 | 0.6 | 0.7 | 0.8 | 0.9 | 1 |
| 30 | 10% | CLP | 6.521 | 6.960 | 8.507 | 10.037 | 11.458 | 12.537 | 12.926 |
| | | PSS | 7.754 | 10.056 | 11.841 | 13.604 | 15.023 | 16.027 | 16.373 |
| | | ASD | 7.027 | 8.196 | 9.856 | 11.460 | 12.895 | 13.951 | 14.319 |
| | 20% | CLP | 6.630 | 7.296 | 8.822 | 10.350 | 11.804 | 12.948 | 13.374 |
| | | PSS | 7.895 | 8.213 | 12.372 | 14.189 | 15.734 | 16.865 | 17.263 |
| | | ASD | 7.680 | 9.965 | 11.742 | 13.503 | 15.040 | 16.177 | 16.576 |
| | 30% | CLP | 6.720 | 7.814 | 9.283 | 10.829 | 12.310 | 13.504 | 13.976 |
| | | PSS | 8.008 | 11.079 | 12.940 | 14.770 | 16.408 | 17.635 | 18.072 |
| | | ASD | 8.329 | 11.968 | 13.936 | 15.822 | 17.494 | 18.729 | 19.155 |

buckling load also increases. This effect is particularly noticeable under ASD and PSS loadings patterns, as these loading types directly apply force or displacement to the stringers.

It should be noted that in oval sections, owing to the asymmetry of the transverse sections, the pre-buckling stress distribution in the transverse sections becomes important in addition to the longitudinal stress distribution. To address this issue, the longitudinal pre-buckling stress distribution in oval sections was investigated using four distinct elements. These elements comprise two sections of the shell and two sections of stringers, positioned as illustrated in Fig. 20. It is evident that the considered elements consist of a stiffener along the major diameter of the oval section (b) and the associated shell element (a) as well as another stiffener along the minor diameter of the oval section (d) and the corresponding shell element (c).

In Fig. 21, a comparison of pre-buckling stresses in shell elements (a) and (c) reveals that the pre-buckling stresses near the minor radius exhibit higher values than those near the major shell radius. This difference is more pronounced in the middle longitudinal sections of the shell.

When comparing pre-buckling stresses in stiffener elements (b) and (d) under CLP and ASD loadings (Fig. 21b and 21d), it is observed that the maximum values are concentrated in the middle longitudinal sections of stringers. Additionally, the pre-buckling stress in section (d) is higher in the middle longitudinal levels than the corresponding pre-buckling stress in section (b). cylinder subjected to PSS loading exhibits the highest pre-buckling stresses in the upper longitudinal sections of the stiffener elements. In oval cross-section cylinders, these stresses are notably higher in stiffeners located near the minor diameter compared to those near the major diameter. The concentration of pre-buckling stress in the upper sections (particularly adjacent to the minor radius) indicates that local buckling is more likely to initiate in stringers positioned along the minor diameter of the shell, To achieve greater comprehensive understanding of the pre-buckling stress distribution in oval sections, Fig. 22(a) shows the pre-buckling stress distribution for oval shells with a b/a ratio of 0.6 under CLP loading, while Fig. 22(b) presents the corresponding distribution under PSS loading.

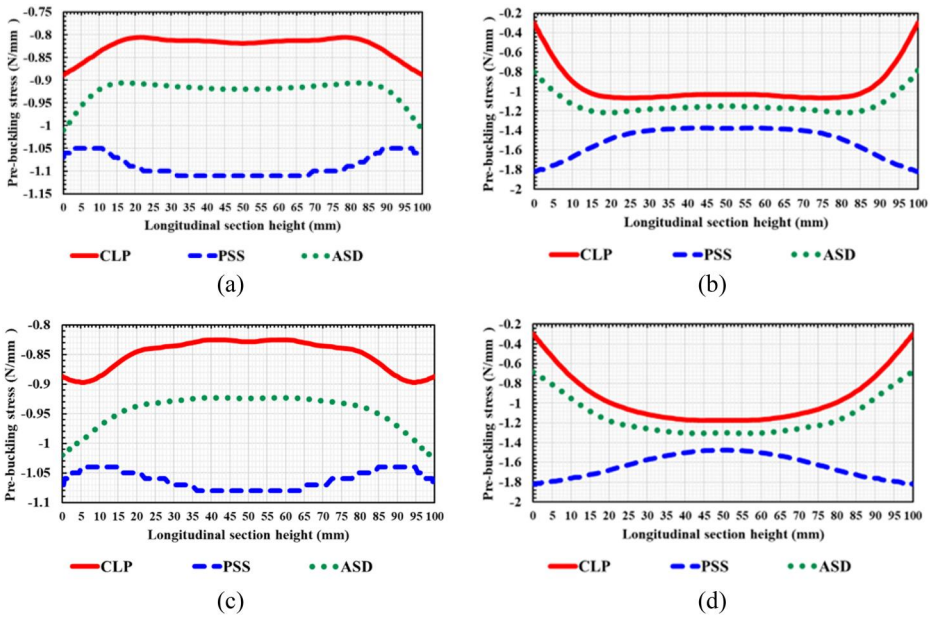


**Figure 21.** Longitudinal pre-buckling stress distribution in elliptical shell with b/a of 0.6 and stiffened by 30 stiffeners with depth of 5 and stiffener area index of 20% (a) Shell element – a section, (b) Stiffener element –b section, (c) Shell element – c section, (d) Stiffener element – d section.

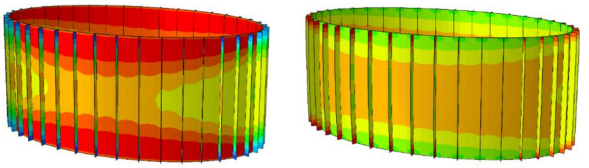

(a) (b)

**Figure 22.** 3D representation of distribution of longitudinal pre-buckling stresses in an oval shell under different loading patterns (a) General buckling of oval shell under CLP loading, (b) Local buckling of oval shell under PSS loading.

**Table 7.** Axial buckling load of composite cylindrical shells with different composite lay-ups under different types of loading (kN/mm).

| | Loading pattern | | | | |
|---|---|---|---|---|---|
| Lay-up | CLP | PSS | ASD | Difference between CLP and PSS buckling loads | Difference between CLP and ASD buckling loads |
| [45, 0, 90, −45] | 537.70 | 361.27 | 362.95 | −32.82% | −33.5% |
| [45, 0, −45, 0] | 400.41 | 438.06 | 466.11 | 9.5% | 16.4% |
| $[90, 0]_s$ | 351.72 | 417.05 | 402.34 | 18.6% | 14.4% |
| [45, 90, −45, 90] | 339.48 | 255.07 | 214.85 | −24.86% | −36.71% |
| $[45, -45]_2$ | 202.68 | 167.12 | 159.16 | −17.54% | −21.47% |
| $[90, 0]_2$ | 299.74 | 358.92 | 346.50 | 19.74% | 15.6% |

In Fig. 22, it is evident that the pre-buckling stresses in the sections of both the shell and stiffener on the side of the minor diameter of the oval exhibit higher values. When comparing shells under different loadings, the shell subjected to CLP loading (illustrated in Fig. 22a) experiences general buckling. The stress in the higher longitudinal sections of the shell surpasses stress in the middle longitudinal sections, and within the stiffener sections, pre-buckling stresses decrease in the higher longitudinal sections before gradually reaching their maximum in the middle longitudinal sections. In contrast, local buckling under the influence of PSS loading (illustrated in Fig. 22b) is distinctly visible. Unlike the CLP loading pattern, Stress reaches its peak value in the upper longitudinal sections of the stiffeners and in the central longitudinal sections of the shell.

### 4.6. Composite layup and number of plies

In the first and second sub-sections of this section, the effects of variation of composite layup and number of plies on the influence of pre-buckling stress distribution on buckling load of the shell subjected to three loading patterns were investigated, respectively.

#### 4.6.1. Composite layup

In this section, the effect of variation of composite layup on the influence of pre-buckling stress distribution on buckling load of the shell is investigated. Table 7 presents the buckling load of composite shell under different loading cases. Moreover, the difference between the buckling loads of the shell under various types of loading (CLP, PSS, and ASD) is provided in this table. As presented in Table 7, composite layup has a significant effect on the difference between buckling loads of the shell under different loading cases.

As shown in Table 7, the composite lay-up with the stacking sequence of $[45, 0, 90, -45]$ exhibits the highest buckling load under the CLP loading pattern, outperforming the other evaluated lay-up configurations. In contrast, the lay-up with the sequence $[45, -45]_2$ demonstrates the lowest buckling load, indicating it is the least effective configuration under the same loading conditions. However, under PSS and ASD loading patterns, the buckling load for this sequence drops significantly. Specifically, there is a 32.82% reduction in buckling load under PSS loading, and a

slightly larger decrease of approximately 33.50% under ASD loading. This reduction can be attributed to the buckling of the stringer and the overall structural weakness of this lay-up when subjected to direct pressure on the stringer, either through applied load (PSS) or imposed displacement (ASD). In comparison, the lay-up with the sequence $[45, -45]_2$ exhibits a lower buckling resistance, making it one of the less effective configurations under the examined loading conditions. However, in some of the other composite lay-up sequences, such as $[45, 0, -45, 0]$ and $[90, 0]_2$, the application of axial pressure directly on the stringer, as in PSS and ASD loading, can actually enhance the buckling performance. This improvement is attributed to the orientation of the plies, which provides greater resistance to these specific types of loading. Among the evaluated sequences, the $[45, 0, -45, 0]$ lay-up exhibits the highest buckling load under PSS and ASD loading conditions, indicating favorable performance when pressure is applied to the stringer. Furthermore, the $[90, 0]_2$ sequence shows the most significant improvement under such loading, with a 19.74% increase in buckling load under PSS and a 15.6% increase under ASD. These findings suggest that among six analyzed lay-up sequences, different configurations may be optimal depending on the loading condition: some perform best when pressure is not applied to the stringer, while others exhibit improved buckling resistance under direct stringer loading. This highlights the importance of selecting the appropriate lay-up sequence based on the expected loading environment.

Figures 23 and 24 present the longitudinal pre-buckling stress distributions of six cylindrical composite specimens that differ only in their laminate layup configurations. Figure 23 illustrates the stress distribution within the shell section, while Fig. 24 shows the corresponding distribution within the stringer section.

In Figs. 23(a) and 24(a), the layup is $[45, 0, -45, 0]$. Figures 23(b) and 24(b) show results for the $[90, 0]_2$ layup. Figures 23(c) and 24(c) correspond to the $[90, 0]_2$ configuration. In Figs. 23(d) and 24(d), the laminate sequence is $[45, 90, -45, 90]$. Figures 23(e) and 24(e) display results for the symmetric layup $[45, -45]_2$. Lastly, Figs. 23(f) and 24(f) represent the outcomes obtained for $[45, 0, 90, -45]$ configuration.

Under the CLP condition in Fig. 23, all subplots show that the higher and lower longitudinal sections of the shell experience greater pre-buckling stress compared to the mid-sections. This trend is consistent across all laminate configurations. For the PSS and ASD loading conditions, a similar stress distribution pattern is observed in Fig. 23(a) $[45, 0, -45, 0]$, Fig. 23(d) $[45, 90, -45, 90]$, Fig. 23(e) $[45, -45]_2$, and Fig. 23(f) $[45, 0, 90, -45]$, where the outer longitudinal regions (top and bottom) show higher stress levels than the middle region of the shell.

However, in Fig. 23(b) $[90, 0]_2$ and Fig. 23(c) $[90, 0]_s$, the ASD loading condition results in a more uniform longitudinal stress distribution across all shell sections. In contrast, under the PSS loading condition for these two configurations, the pre-buckling stress is actually lower in the higher and lower longitudinal sections than in the mid-section, indicating a reversed stress gradient.

Another notable observation is the variation in the magnitude of stress difference between the outer and mid-longitudinal regions. The difference observed in Fig. 23(a) $[45, 0, -45, 0]$ and Fig. 23(b) $[90, 0]_2$ is the smallest among all six layups, with the stress variation between the high/low and mid-longitudinal sections being approximately 10%. In contrast, Fig. 23(e) $[45, -45]_2$ exhibits the largest disparity, showing about a 50% difference between the same regions.

For the stringer sections shown in Fig. 24, an opposite trend to the shell sections can be observed. Under the CLP loading condition, all laminate configurations exhibit lower pre-buckling stress in the higher and lower longitudinal regions of the shell compared to the mid-sections. When load is applied directly to the stringers, either through PSS or ASD, a significant increase in stress within the stringer sections is evident, as the load is transferred directly into the stringers. Under ASD loading, the stress in the stringer sections generally remains lower in the higher and lower regions than in the mid-sections of the shell. However, an exception is seen in

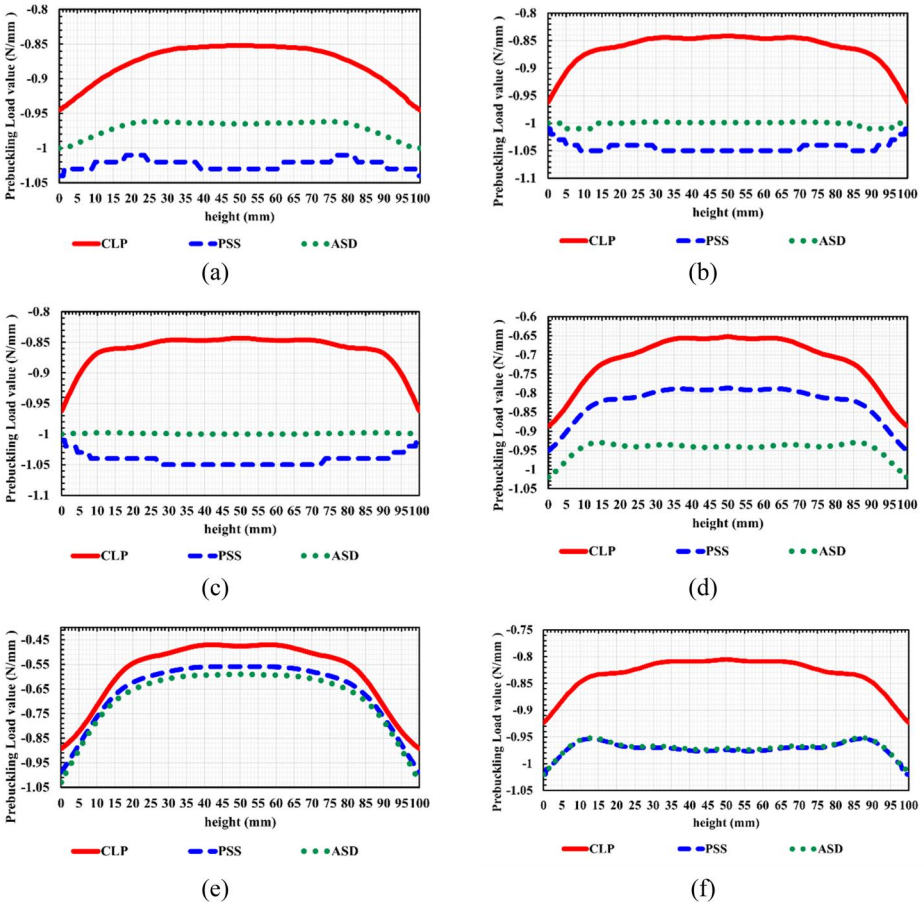


**Figure 23.** Longitudinal pre-buckling stress distribution on shell considering stringer depth of 5 and different composite lay-ups (a) [45, 0, −45, 0], (b) $[90, 0]_2$ (c) $[90, 0]_s$, (d) (Ogunleye et al. 2022; 90; Ogunleye et al. 2022; 90), (e) $[45, -45]_2$ (f) [45, 0, 90, −45].

Fig. 24(b) $[90, 0]_2$ and Fig. 24(c) $[90, 0]_s$, where ASD loading results in a more uniform stress distribution across all longitudinal sections. Conversely, under PSS loading, these same configurations display higher pre-buckling stress in the upper and lower longitudinal sections than in the middle. This phenomenon may be influenced by the depth of the stringers, as discussed in previous sections, greater stringer depth increases the likelihood that stress in the higher and lower sections exceeds that in the mid-section of the shell.

Regarding the difference in stress between different longitudinal regions of the shell, it can be observed that when no direct load is applied to the stringers, the stress in the upper and lower sections remains relatively low, typically in the range of 0–0.2, because the stress is indirectly transferred to the stringer from the shell. This load transfer is more concentrated in the mid-section, which is typically where general buckling tends to initiate.

Figure 25 illustrates the buckling mode shapes of the stiffened cylindrical shell for three composite layups ($[45, -45]_2$, $[90, 0]_s$, and $[45, 0, 90, -45]$) under three different loading conditions: CLP, ASD, and PSS. The shell structure includes longitudinal stringers designed with a stringer area index of 10% relative to the total shell surface area, and a stringer depth of 7 mm. This relatively weak stiffening layout was intentionally selected to allow for a clearer comparison of the buckling behavior across the different layup configurations.

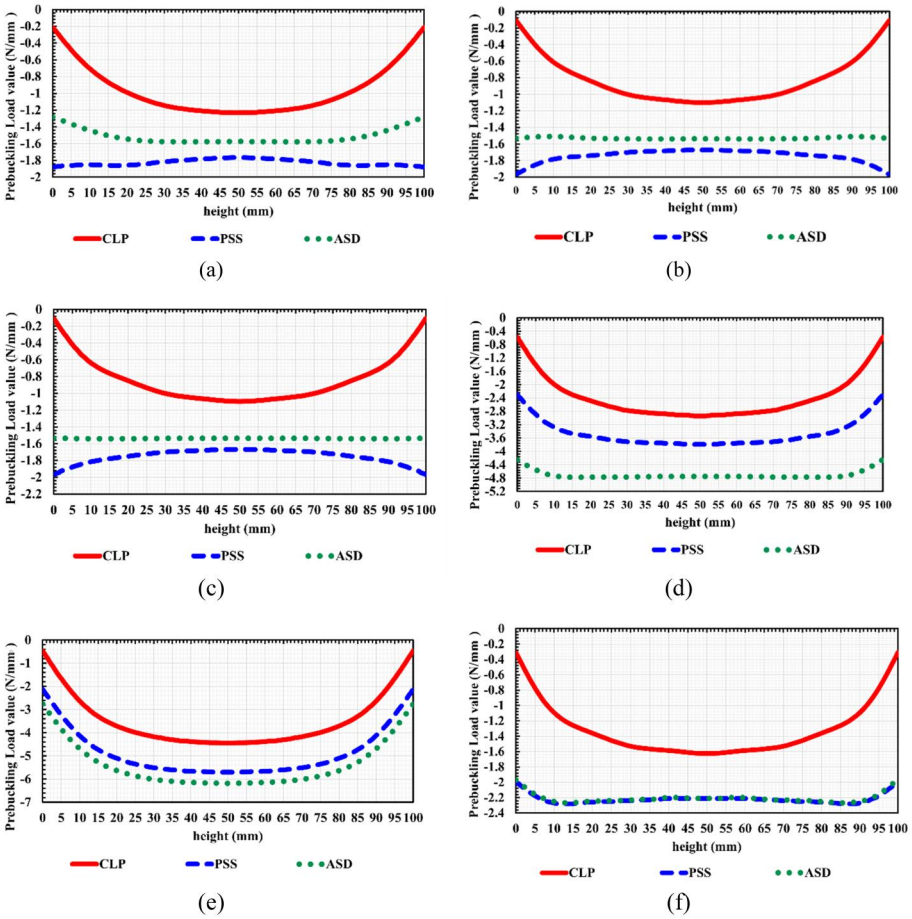


**Figure 24.** Longitudinal pre-buckling stress distribution on stringer element considering stringer depth of 5 and different composite lay-ups (a) [45, 0, −45, 0], (b) $[90, 0]_2$ (c) $[90, 0]_s$, (d) (Ogunleye et al. 2022; 90; Ogunleye et al. 2022; 90), (e) $[45, -45]_2$ (f) [45, 0, 90, −45].

Figure 25(a), 25(b), and 25(c) corresponds to the $[45, -45]_2$ layup under CLP, ASD, and PSS loading, respectively. Figure 25(d), 25(e), and 25(f) shows the buckling results for the $[90, 0]_s$ configuration, while Fig. 25(g), 25(h), and 25(i) displays the response for the $[45, 0, 90, -45]$ layup. The differences in buckling mode shapes among the various layups and loading conditions reinforce the trends and analyses discussed in this section.

An assessment of the buckling mode shapes in Fig. 25 reveals distinct behaviors across the loading conditions and composite layups. Under CLP loading (shown in Fig. 25(a), 25(d), and 25(g)), corresponding to the $[45, -45]_2$, $[90, 0]_s$, and $[45, 0, 90, -45]$ layups, respectively, only the (90°, 0°, 0°, 90°) configuration does not exhibit local buckling. In contrast, for the other two layups, local buckling is evident, particularly in the mid-surface regions of the stringers. This behavior indicates that the shell stress is effectively transferred into the stringers, leading to localized instability and buckling in these areas. However, under ASD loading, only the $[90, 0]_s$ layup (Fig. 25(f)) demonstrates resistance to local buckling, while the other two configurations (including $[45, -45]_2$ and $[45, 0, 90, -45]$) as shown in Fig. 25(c) and 25(i), clearly exhibit localized buckling patterns. Under PSS loading, all three layups $[45, -45]_2$ in Fig. 25(b), $[90, 0]_s$ in Fig. 25(e), and $[45, 0, 90, -45]$ in Fig. 25(h), display pronounced local buckling, confirming the influence of direct pressure loading on the onset of localized deformation in the stiffened shell structures.

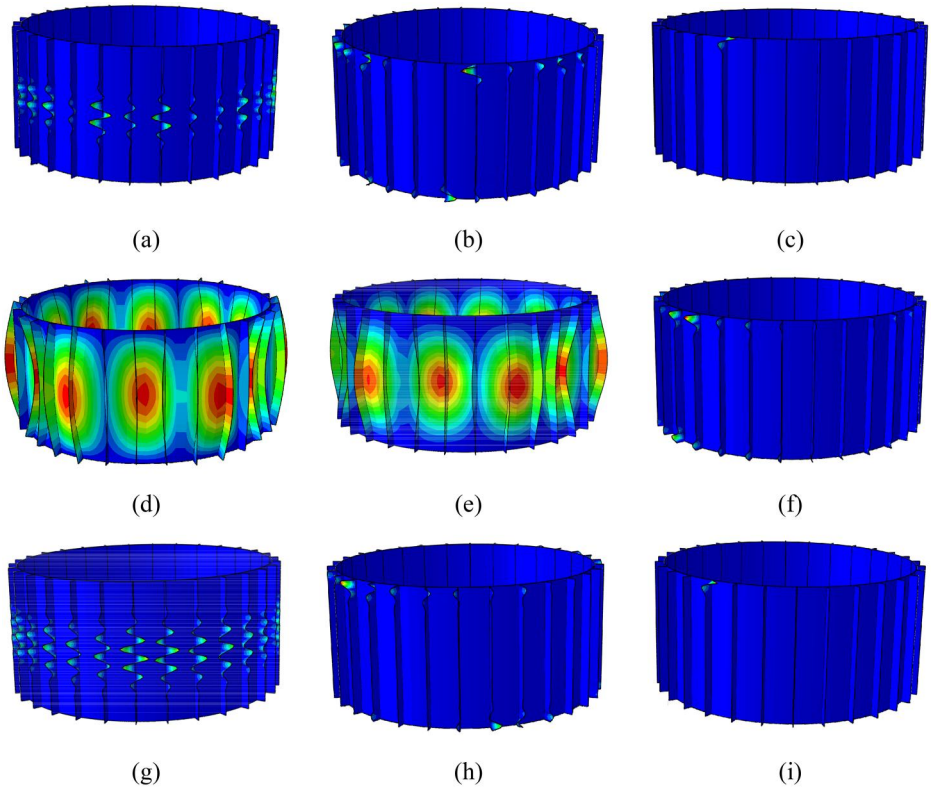


**Figure 25.** Buckling mode shape of composite cylindrical shells under different types of loading (a) $[45, -45]_2$ – CLP, (b) $[45, -45]_2$ – PSS, (c) $[45, -45]_2$ – ASD, (d) $[90,0]_s$ – CLP, (e) $[90,0]_s$ – PSS, (f) $[90,0]_s$ – ASD, (g) [45,0,90,−45] – CLP, (h) [45,0,90,−45] – PSS, (i) [45,0,90,−45] – ASD.

**Table 8.** Effect of number of plies on buckling load of shell (kN/mm).

| Lay up | Number of plies | CLP | PSS | ASD |
|---|---|---|---|---|
| $[90, 0]_2$ | 4 | 362.755 | 445.323 | 482.088 |
| $(90, 0]_s$ | 4 | 428.013 | 509.313 | 525.192 |
| $[45, -45]_2$ | 4 | 361.837 | 440.241 | 444.749 |
| $[90,0]_3$ | 6 | 377.226 | 457.795 | 495.133 |
| $(90, 0, 90)_s$ | 6 | 400.173 | 477.506 | 558.168 |
| $[45, -45]_3$ | 6 | 361.827 | 440.231 | 444.801 |
| $[90, 0]_4$ | 8 | 383.257 | 463.058 | 500.883 |
| $[90, 0]_{2s}$ | 8 | 413.168 | 493.111 | 533.940 |
| $[45, -45]_4$ | 8 | 361.828 | 440.226 | 444.760 |

### *4.6.2. Number of plies*

The effect of number of plies on the buckling load and mode shape of the shell subjected to three loading patterns was investigated in this section. In this regard, as presented in Table 8, three different composite layups having three different number of plies (4, 6 and 8) were considered. The thickness of the shell in all cases is considered as 1. Table 8 presents the effect of number of plies on buckling load of the shell for all cases.

For the $[90, 0]_n$ layup series (specifically $[90, 0]_2$, $[90, 0]_3$, and $[90, 0]_4$, corresponding to 4, 6, and 8 plies, respectively), an increase in the number of plies results in a notable improvement in buckling resistance. Although the total laminate thickness remains the same, the increase in ply count reduces individual ply thickness, potentially improving interlaminar load transfer and delaying the onset of local instabilities, thereby enhancing the overall structural performance.

In contrast, the $[45, -45]_n$ layup series (tested in 4, 6, and 8-ply forms) shows negligible variation in critical buckling load with increasing ply number. This suggests that, for laminates composed solely of ±45 orientations, increasing the number of thinner plies does not significantly influence axial or shear stiffness, resulting in nearly identical buckling behavior regardless of ply count.

When comparing symmetric layups, the 4-ply configuration $[90, 0]_s$ exhibits the highest buckling load among the 4-ply group, reflecting the advantage of balanced axial stiffness and reduced coupling effects. In the 6-ply group, the symmetric layup $[90, 0, 90]_s$ also demonstrates strong buckling performance; however, it cannot be directly compared with the 4-ply symmetric layup due to the difference in stacking sequence and ply count. Similarly, the 8-ply symmetric configuration $[90, 0]_{2s}$ shows high performance but should not be directly evaluated against the 6-ply layup, as the stacking sequences differ. These observations highlight that while symmetry generally contributes positively to structural stability, the specific arrangement and orientation of plies play a critical role in defining the buckling response.

Overall, for a fixed laminate thickness, the results indicate that increasing the number of plies can enhance buckling performance for certain layups (particularly those with axial fiber components) by improving stress distribution and delaying failure mechanisms. However, in layups dominated by off-axis plies such as ±45, this trend does not hold, highlighting the importance of fiber orientation in tailoring buckling resistance.

## 5. Conclusion

A comprehensive literature review underscores that the stress distribution during the pre-buckling phase significantly influences the buckling load of structures obtained from eigenvalue approach. This issue was neglected in the buckling of stiffened shell structures. To address this issue, a FSM was employed to simulate the stringer-stiffened elliptical cylindrical shell, considering three distinct types of pre-buckling stress distributions within the model. These pre-buckling stress distributions include (1) applying uniformly distributed axial pressure to the shell edge (CLP), (2) applying a uniformly distributed axial pressure to the edges of the shell and stringers (PSS) and (3) applying same axial end-shortening to edges of shell and stringers (ASD). In this modeling approach, the stringers have been simulated as discrete components of the shell. This particular modeling strategy enables a precise examination of the impact of three applied loading models on the stress generated and distributed within the stringers. The model's results were validated by comparing them with findings from previous studies. A comprehensive assessment was conducted through a parametric study, investigating the influences of various parameters, including the number of stringers, stringer depth, stringer area index, cross-section of the shell (b/a), and length of the shell, on the pre-buckling stress induced on both the stringers and the shell, resulting in buckling within the shell and stringers. The results obtained from the parametric study are summarized as follows:

- Increasing the depth of the stringers leads to the increasing the longitudinal stress value in the stringer specifically in cases of ASD and PSS due to increase in slenderness ratio of stringers. In these manners, the local buckling is happened in the stringers and accordingly, the buckling load of the stiffened shell structure decreases significantly.
- Increasing the stringer area index leads to decreasing the possibility of localized buckling in the stringers due to increases in stringers thickness and reducing the slenderness ratio of stringer elements. Accordingly, as the stringer area index increases, the buckling load of stiffened structure increases.
- Number of stringers has a significant on the buckling of shell structure. For a constant stringer area index, as the number of stringers increases, the thickness of stringers decreases

and the bucking load of the structure decreases due to local buckling of stringers. However, in instances where local buckling is not observed in the stringers, an increase in their quantity can contribute to an elevation in the overall structural buckling load.

- In elliptical cylindrical shells, the value of longitudinal stress induced in sections near the minor diameter is highly more than that for the section near the major diameter. Accordingly, for the elliptical cylindrical shells, buckling is usually occurred in the sections near the minor diameter.
- Composite layup orientation and ply number play critical roles in determining buckling behavior of composite stiffened cylindrical shells. Optimal fiber alignment enhances buckling load-specific performance, while increasing ply count, particularly in axially aligned configurations, improves buckling resistance by promoting better stress distribution and delaying instability.

From a design efficiency standpoint, engaging the stringers in load-bearing, especially under ASD-type loading, can improve the buckling capacity of the structure. However, excessive loading on slender stringers (i.e., those with high depth-to-thickness ratios) may lead to premature local buckling. Therefore, in scenarios where local buckling is a concern, or where stringer geometry is limited due to manufacturing constraints, a CLP loading pattern may offer a more conservative and cost-effective solution. Conversely, if enhancing the overall buckling strength is prioritized, ASD loading type, assuming stringers are appropriately designed to avoid local instabilities, can be leveraged to maximize structural performance. This guideline highlights that the choice of loading condition in design should be informed by a balance between manufacturing feasibility, cost, and desired structural performance. In real-life applications, CLP and ASD are the most practically applicable, with ASD offering higher performance when carefully managed.

The main limitation of this study is the use of a linear eigenvalue buckling analysis, which inherently neglects the presence of geometric imperfections and post-buckling nonlinearities. While this approach allows efficient exploration of the influence of design variables such as stringer slenderness and stress distribution, it cannot fully capture the imperfection-sensitivity of thin-walled shell structures. The findings should therefore be interpreted as idealized trends. For applications requiring high-fidelity predictions of collapse loads, it is recommended that future research incorporate geometrical nonlinear analysis or Koiter's theory with initial imperfections modeled according to established standards or measured data.

## Disclosure statement

No potential conflict of interest was reported by the authors.

## Funding

This work was supported by the Shahid Chamran University of Ahvaz (SCU) [SCU.C1403.530].

## Data availability statement

Data will be made available on request.

## References

Asadi, E., and M. S. Qatu. 2012. "Static Analysis of Thick Laminated Shells with Different Boundary Conditions Using GDQ." *Thin-Walled Structures* 51: 76–81. https://doi.org/10.1016/j.tws.2011.11.004

ASTM International. 2016. *ASTM D6641/D6641M-16: Standard Test Method for Compressive Properties of Polymer Matrix Composite Materials Using a Combined Loading Compression (CLC) Test Fixture*. West Conshohocken, PA: ASTM International.

Azzuni, E., and S. Guzey. 2018. "A Perturbation Approach on Buckling and Postbuckling of Circular Rings under Nonuniform Loads." *International Journal of Mechanical Sciences* 137: 86–95. https://doi.org/10.1016/j.ijmecsci.2018.01.004

Barbero, E. J., A. Madeo, G. Zagari, R. Zinno, and G. Zucco. 2017. "Imperfection Sensitivity Analysis of Composite Cylindrical Shells Using Koiter's Method." *International Journal for Computational Methods in Engineering Science and Mechanics* 18 (1): 105–111. https://doi.org/10.1080/15502287.2016.1276359

Bich, D. H., D. Van Dung, V. H. Nam, and N. T. Phuong. 2013. "Nonlinear Static and Dynamic Buckling Analysis of Imperfect Eccentrically Stiffened Functionally Graded Circular Cylindrical Thin Shells under Axial Compression." *International Journal of Mechanical Sciences* 74: 190–120. https://doi.org/10.1016/j.ijmecsci.2013.06.002

Clark, J. W., and A. H. Knoll. 1958. "Effect of Deflection on Lateral Buckling Strength." *Journal of the Engineering Mechanics Division* 84 (2): 1596–1591. https://doi.org/10.1061/JMCEA3.0000060

Duc, N. D., N. D. Tuan, P. Tran, P. H. Cong, and P. D. Nguyen. 2016. "Nonlinear Stability of Eccentrically Stiffened S-FGM Elliptical Cylindrical Shells in Thermal Environment." *Thin-Walled Structures* 108: 280–290. https://doi.org/10.1016/j.tws.2016.08.025

Duc, N. D., P. D. Nguyen, and N. D. Khoa. 2017. "Nonlinear Dynamic Analysis and Vibration of Eccentrically Stiffened S-FGM Elliptical Cylindrical Shells Surrounded on Elastic Foundations in Thermal Environments." *Thin-Walled Structures* 117: 178–189. https://doi.org/10.1016/j.tws.2017.04.013

Dung, D. V., and L. K. Hoa. 2013. "Nonlinear Buckling and Post-Buckling Analysis of Eccentrically Stiffened Functionally Graded Circular Cylindrical Shells under External Pressure." *Thin-Walled Structures* 63: 117–124. https://doi.org/10.1016/j.tws.2012.09.010

Ghorbanpour Arani, A., A. Loghman, A. A. Mosallaie Barzoki, and R. Kolahchi. 2010. "Elastic Buckling Analysis of Ring and Stringer-Stiffened Cylindrical Shells under General Pressure and Axial Compression via the Ritz Method." *Journal of Solid Mechanics* 2 (4): 332–347. https://journals.iau.ir/article_514389.html

Golchi, M., M. Talebitooti, and R. Talebitooti. 2019. "Thermal Buckling and Free Vibration of FG Truncated Conical Shells with Stringer and Ring Stiffeners Using Differential Quadrature Method." *Mechanics Based Design of Structures and Machines* 47 (3): 255–282. https://doi.org/10.1080/15397734.2018.1545588

Hancock, G. J., and C. H. Pham. 2017. "Analyses of Thin-Walled Sections under Localised Loading for General End Boundary Conditions–Part 1: Pre-Buckling." *Thin-Walled Structures* 119: 956–972. https://doi.org/10.1016/j.tws.2017.01.010

Jiao, P., Z. Chen, H. Ma, H. Miao, and H. Ou. 2023. "Buckling Behavior Analysis of Thin-Walled Cylindrical Shell Structure under Localized Axial Compression Load Based on Initial Imperfection Sensitivity." *International Journal of Structural Stability and Dynamics* 23 (20): 2350197. https://doi.org/10.1142/S0219455423501973

Jones, R. M. 2018. *Mechanics of Composite Materials*. Boca Raton, FL: CRC Press. https://doi.org/10.1201/9781498711067

Kabir, M. Z. and D. Poorveis. 2006. "Buckling of Discretely Stringer-Stiffened Composite Cylindrical Shells under Combined Axial Compression and External Pressure." *Scientia Iranica* 13 (2): 113–123. https://scientiairanica.sharif.edu/article_2569.html

Khajehdezfuly, A., D. Poorveis, and S. Nazarinia. 2023. "Comparison between Linear and Nonlinear Buckling Loads of FGM Cylindrical Panel with Cutout." *International Journal of Non-Linear Mechanics* 150: 104361. https://doi.org/10.1016/j.ijnonlinmec.2023.104361

Khayat, M., D. Poorveis, and S. Moradi. 2016. "Buckling Analysis of Laminated Composite Cylindrical Shell Subjected to Lateral Displacement-Dependent Pressure Using Semi-Analytical Finite Strip Method." *Steel and Composite Structures* 22 (2): 301–321. https://doi.org/10.12989/scs.2016.22.2.301

Khayat, M., D. Poorveis, and S. Moradi. 2017. "Buckling Analysis of Functionally Graded Truncated Conical Shells under External Displacement-Dependent Pressure." *Steel and Composite Structures* 23 (1): 1–16. https://doi.org/10.12989/scs.2017.23.1.001

Kumar, R., A. Lal, and B. M. Sutaria. 2023. "Buckling of Laminated Composite Plate with Various Shapes of Holes under Uniform/Nonuniform Mechanical and Thermal Loading." *Plastics, Rubber and Composites* 52 (7): 387–401. https://doi.org/10.1080/14658011.2023.2207061

Lai, A. D., J. F. Jia, J. L. Qu, J. Y. Wang, J. B. Sun, Z. H. Zhou, X. S. Xu, and C. W. Lim. 2023. "Local–Global Buckling of Cylindrical Shells with Wall Thinning Defects." *Mechanics Based Design of Structures and Machines* 51 (5): 2481–2500. https://doi.org/10.1080/15397734.2021.1899830

Moradi, A., D. Poorveis, and A. Khajehdezfuly. 2022. "Buckling of FGM Elliptical Cylindrical Shell under Follower Lateral Pressure." Steel and Composite Structures *An International Journal* 45 (2): 175–191. https://doi.org/10.12989/scs.2022.45.2.175

NASA. 1968. *Buckling of Thin-Walled Circular Cylindrical Shells* (SP8007). Washington, DC: National Aeronautics and Space Administration.

Nguyen, H. L. T., I. Elishakoff, and V. T. Nguyen. 2009. "Buckling under the External Pressure of Cylindrical Shells with Variable Thickness." *International Journal of Solids and Structures* 46 (24): 4163–4168. https://doi.org/10.1016/j.ijsolstr.2009.07.025

Nguyen, T. N., D. Zhang, M. Mirrashid, D. K. Nguyen, and P. Singhatanadgid. 2024. "Fast Analysis and Prediction Approach for Geometrically Nonlinear Bending Analysis of Plates and Shells Using Artificial Neural Networks." *Mechanics of Advanced Materials and Structures* 31 (28): 10221–10239. https://doi.org/10.1080/15376494.2023.2286626

Nguyen, T. P., M. D. Vu, T. D. Dang, V. D. Cao, T. H. Pham, and H. N. Vu. 2023. "An Analytical Approach of Nonlinear Buckling Behavior of Torsionally Loaded Auxetic Core Toroidal Shell Segments with Graphene Reinforced Polymer Coatings." *Advanced Composite Materials* 32 (3): 400–418. https://doi.org/10.1080/09243046.2022.2110661

Ogunleye, R. O., S. Rusnakova, M. Zaludek, and S. Emebu. 2022. "The Influence of Ply Stacking Sequence on Mechanical Properties of Carbon/Epoxy Composite Laminates." *Polymers* 14 (24): 5566. https://doi.org/10.3390/polym14245566

Ovesy, H. R., and J. Fazilati. 2012. "Buckling and Free Vibration Finite Strip Analysis of Composite Plates with Cutout Based on Two Different Modeling Approaches." *Composite Structures* 94 (3): 1250–1258. https://doi.org/10.1016/j.compstruct.2011.11.009

Patel, M., L. Sonkar, and S. Patel. 2025. "Assessment of Ply Stacking Sequence Effect on Damage Behavior of CFRP Composite Laminate Under Low-Velocity Impacts." *Advances in Materials Science and Engineering* 2025 (1): 4349535. https://doi.org/10.1155/amse/4349535

Pezeshky, P., and M. Mohareb. 2018. "Distortional Lateral Torsional Buckling of Beam-Columns Including Pre-Buckling Deformation Effects." *Computers & Structures* 209: 93–116. https://doi.org/10.1016/j.compstruc.2018.08.010

Pi, Y. L., and M. A. Bradford. 2010. "Effects of Prebuckling Analyses on Determining Buckling Loads of Pin-Ended Circular Arches." *Mechanics Research Communications* 37 (6): 545–553. https://doi.org/10.1016/j.mechrescom.2010.07.016

Poorveis, D., A. Khajehdezfuly, M. R. Sardari, and S. Moradi. 2024. "An Accurate Approach for Buckling Analysis of Stringer Stiffened Laminated Composite Cylindrical Shells under Axial Compression." *Steel and Composite Structures* 51 (5): 543–562. https://doi.org/10.12989/scs.2024.51.5.545

Poorveis, D., A. Khajehdezfuly, S. Moradi, and E. Shirshekan. 2019. "A Simple Spline Finite Strip for Buckling Analysis of Composite Cylindrical Panel with Cutout." *Latin American Journal of Solids and Structures* 16 (8): 1–26. https://doi.org/10.1590/1679-78255535

Ramachandra, L. S., T. Dey, and R. Kumar. 2022. "Stability of Plates and Shell Panels under Non-Uniform in-Plane Loadings." In *Stability and Failure of High Performance Composite Structures*, 143–165. Singapore: Springer Nature Singapore. https://doi.org/10.1007/978-981-19-2424-8_7

Reddy, J. N. 2006. *Theory and Analysis of Elastic Plates and Shells*. Boca Raton, FL: CRC Press.

Sadeghifar, M., M. Bagheri, and A. A. Jafari. 2010. "Multiobjective Optimization of Orthogonally Stiffened Cylindrical Shells for Minimum Weight and Maximum Axial Buckling Load." *Thin-Walled Structures* 48 (12): 979–988. https://doi.org/10.1016/j.tws.2010.07.006

Sadeghifar, M., M. Bagheri, and A. A. Jafari. 2011. "Buckling Analysis of Stringer-Stiffened Laminated Cylindrical Shells with Nonuniform Eccentricity." *Archive of Applied Mechanics* 81 (7): 875–886. https://doi.org/10.1007/s00419-010-0457-0

Salahshour, S., and F. Fallah. 2018. "Elastic Collapse of Thin Long Cylindrical Shells under External Pressure." *Thin-Walled Structures* 124: 81–87. https://doi.org/10.1016/j.tws.2017.11.058

Shahgholian-Ghahfarokhi, D., M. Safarpour, and A. Rahimi. 2021. "Torsional Buckling Analyses of Functionally Graded Porous Nanocomposite Cylindrical Shells Reinforced with Graphene Platelets (GPLs)." *Mechanics Based Design of Structures and Machines* 49 (1): 81–102. https://doi.org/10.1080/15397734.2019.1666723

Silvestre, N. 2008. "Buckling Behaviour of Elliptical Cylindrical Shells and Tubes under Compression." *International Journal of Solids and Structures* 45 (16): 4427–4447. https://doi.org/10.1016/j.ijsolstr.2008.03.019

Taig, G., G. Ranzi, and A. Luongo. 2016. "GBT Pre-Buckling and Buckling Analyses of Thin-Walled Members under Axial and Transverse Loads." *Continuum Mechanics and Thermodynamics* 28 (1–2): 41–66. https://doi.org/10.1007/s00161-014-0399-9

Teng, J. G., and T. Hong. 1998. "Nonlinear Thin Shell Theories for Numerical Buckling Predictions." *Thin-Walled Structures* 31 (1–3): 89–115. https://doi.org/10.1016/S0263-8231(98)00014-7

Tornabene, F., and E. Viola. 2009. "Free Vibration Analysis of Functionally Graded Panels and Shells of Revolution." *Meccanica* 44 (3): 255–281. https://doi.org/10.1007/s11012-008-9167-x

Vu, H. N., T. P. Nguyen, S. L. Ho, M. D. Vu, and V. D. Cao. 2023. "Nonlinear Buckling Analysis of Stiffened FG-GRC Laminated Cylindrical Shells Subjected to Axial Compressive Load in Thermal Environment." *Mechanics Based Design of Structures and Machines* 51 (7): 3678–3694. https://doi.org/10.1080/15397734.2021.1932522

Wang, B., M. Yang, D. Zeng, P. Hao, G. Li, Y. Liu, and K. Tian. 2021. "Post-Buckling Behavior of Stiffened Cylindrical Shell and Experimental Validation under Non-Uniform External Pressure and Axial Compression." *Thin-Walled Structures* 161: 107481. https://doi.org/10.1016/j.tws.2021.107481

Wang, C. M., K. M. Liew, Y. Xiang, and S. Kitipornchai. 1992. "Application of Trefftz Theory in Thin-Plate Buckling with in-Plane Pre-Buckling Deformations." *International Journal of Mechanical Sciences* 34 (9): 681–688. https://doi.org/10.1016/0020-7403(92)90001-W

Wang, Y., C. Feng, Z. Zhao, and J. Yang. 2018. "Eigenvalue Buckling of Functionally Graded Cylindrical Shells Reinforced with Graphene Platelets (GPL)." *Composite Structures* 202: 38–46. https://doi.org/10.1016/j.compstruct.2017.10.005

Xin, J., J. Wang, J. Yao, and Q. Han. 2011. "Vibration, Buckling and Dynamic Stability of a Cracked Cylindrical Shell with Time-Varying Rotating Speed." *Mechanics Based Design of Structures and Machines* 39 (4): 461–490. https://doi.org/10.1080/15397734.2011.569301

Zhang, X., G. Lv, W. Wang, C. Li, H. Miao, and C. Fang. 2024. "Numerical and Experimental Investigation of Pre-Damaged Composite Stiffened Panel under Axial Compression." *Engineering Fracture Mechanics* 309: 110406. https://doi.org/10.1016/j.engfracmech.2024.110406

## Appendix A

This appendix presents the mathematical formulations associated with the CLP and PSS loading patterns. It includes the governing equations, boundary conditions, and load vector definitions specific to each loading case, offering a clear reference for the implementation and analysis described in the main body of this paper.

Equation (A.1) is used to determine the virtual external work ($\delta W_{ext}^{\mathrm{sh}}$) in loading cases 1 and 2, which is caused by the uniform axial pressure applied on the shell edge (or shell and stringer edges in the second case) in the direction of u (Figs. 4 and 5).

$$\delta W_{ext}^{sh} = \int_{s_i}^{s_j} \bar{P}_{sh}(\delta u]_{x=0} - \delta u]_{x=L})ds \tag{A.1}$$

Equation (A.2) is used to derive $\delta u$, which is the virtual axial displacement at location of x. In Eq. (12), s stands for arc length.

$$\delta u = \sum_{p=1}^{M}\sum_{q=1}^{2}\delta u_{pq}N_q(\eta)\cos\left(\frac{p\pi x}{L}\right) + \sum_{q=1}^{2}\delta u_{0q}N_q(\eta)\left(\frac{1}{2} - \frac{x}{L}\right) \tag{A.2}$$

Equation (A.2) is stated as follows: $N_q(\eta)$ is the Lagrangian shape function for the q-th node of a two nodded strip element, and $\eta$ is a dimensionless variable. Using Eq. (A.3), the arc length of an ellipse (s) can be found based on $\eta$.

$$s = \left(\frac{s_j - s_i}{2}\right)\eta + \left(\frac{s_i + s_j}{2}\right) \tag{A.3}$$

Equation (A.3) uses the terms $s_j$ and $s_i$ to represent the arc lengths of the jth and ith nodes, respectively. By calculating s with regard to $\eta$ in Eq. (A.3), Eq. (A.4) was produced.

$$\frac{ds}{d\eta} = \left(\frac{s_j - s_i}{2}\right) \tag{A.4}$$

Equation (A.4) uses the Jacobian (J) notation $\frac{ds}{d\eta}$. Equation 17 can be obtained by replacing Eqs. (A.2) and (A.4) in Eq. (12) to represent the virtual external work ($\delta W_{ext}^{\mathrm{sh}}$) produced by the uniform axial pressure applied on the shell edge ($\bar{P}_{sh}$) in the direction of u (Fig. 5).

$$\delta W_{ext}^{sh} = \int_{-1}^{+1} \bar{P}_{sh}.\left[\sum_{p=1}^{M}\sum_{q=1}^{2}\delta u_{pq}N_q(\eta)\big(1 - \cos(p\pi)\big) + \sum_{q=1}^{2}\delta u_{0q}N_q(\eta)\right] * Jd\eta \tag{A.5}$$

Based on various nodes and harmonics in each strip element, Eq. (A.5) has been shortened to Eq. (A.6).

$$\delta W_{ext}^{sh} = \sum_{p=1}^{M}\sum_{q=1}^{2}\delta u_{pq} * F_{pq,sh}^{u} + \sum_{q=1}^{2}\delta u_{0q} * F_{0q,sh}^{u0} \tag{A.6}$$

Equation (A.6) denotes the number of harmonics (p), the number of nodes (q), the total number of harmonics (M), The portion of load for the $q$th node and $p$th harmonic is represented by $F_{pq,sh}^{u}$, while the portion of axial displacement for the $q$th node and $p$th harmonic is represented by $\delta u_{pq}$. The pre-buckling analysis provided the portion of load for the $q$th node, denoted as $F_{0q,sh}^{u}$, and the portion of axial displacement for the same node, denoted as $\delta u_{0q}$. As a result, Eqs. (A.5) and (A.6) provide the load vectors applied at the edges of each strip element that correspond to all harmonics ($F_{pq,sh}^{u}$) and nodes ($F_{oq,sh}^{u}$). Actually, Eqs. (A.5) and (A.6) provide the load vectors applied at each node that correspond to each harmonic. Stated differently, the external load vectors applied to the edges of each node of each harmonic in the shell in the first and second loading cases are given by Eqs. (A.7) and (A.8).

$$F_{pq,sh}^{u} = \int_{-1}^{+1} \bar{P}_{sh} * \ N_q(\eta)\big(1-\cos(p\pi)\big) * Jd\eta \tag{A.7}$$

$$F_{oq,sh}^{u} = \int_{-1}^{+1} \bar{P}_{sh} * \ N_q(\eta) * Jd\eta \tag{A.8}$$

The external load vector applied to the stringers was ascertained using the same procedure as in the second pre-buckling stress distribution. Thus, using Eqs. (A.9) and (A.10), the external load vectors of stringers corresponding to all nodes ($F_{pq,str}^{u}$) and harmonics nodes ($F_{0q,str}^{u}$) were calculated.

$$F_{pq,str}^{u} = \int_{-1}^{+1} \bar{P}_{str} * \ N_q(\eta)\big(1-\cos(p\pi)\big) * Jd\eta \tag{A.9}$$

$$F_{0q,str}^{u} = \int_{-1}^{+1} \bar{P}_{str} * \ N_q(\eta) * Jd\eta \tag{A.10}$$

$\bar{P}_{str}$ is equal to $\bar{P}_{sh} \times \frac{t_{str}}{t_{sh}}$ in Eqs. (A.9) and (A.10), where $t_{str}$ and $t_{sh}$ represent the stringer and shell thickness, respectively. Furthermore, J is equal to $\frac{h_{st}}{2}$, where $h_{st}$ is the stringer depth.

## Appendix B

This appendix provides the detailed formulation for the ASD loading pattern. It outlines the relevant mathematical expressions, boundary conditions, and the construction of the load vector, serving as a technical supplement to the corresponding analysis in the paper. The third type of pre-buckling stress distribution (ASD) in this study consisted of applying the same axial displacement to the edges of the shell and stringers. Figure 6 is a schematic view of the third loading case. The shell and stringer edges were subjected to the same axial displacement using the penalty approach. The axial displacement of the stringers and shell ends was considered to be $\Delta_0$ (Fig. 3c).

$$u_i]_{x=0} - u_i]_{x=L} = \Delta_0 \tag{B.1}$$

In Eq. (B.1), $i$ denotes the node number of the shell or stringer, which is found on the outside edges of the shell and stringers. A constraint was generated by substituting the extended version of $u$ Eq. (1) in Eq. (B.1), and Eq. (B.2) was assigned to all nodes on the edges of all stringers and shell.

$$\sum_{m=1,3,\ldots}^{M} u_{mi} + \frac{1}{2}u_{0i} = \frac{\Delta_0}{2} \quad i = 1 \ \ to \ \ npoint \tag{B.2}$$

In Eq. (B.2), the terms harmonic number (m) and number of nodes on both shell edges and all stringers (i) are used. The total number of nodes taken into account on the end edges of the shell and all stringers is represented by npoint in Eq. (B.2). The formulation of a "stringer-stiffened shell" as a second-degree constraint using the penalty method Eq. (B.3) was attributed to Eq. (B.2).

$$(Rest)_i = \frac{1}{2} * pen * \left[\sum_{m=1,3,\ldots}^{M} u_{mi} + \frac{1}{2}u_{0i} - \frac{\Delta_0}{2}\right]^2 \tag{B.3}$$

In Eq. (B.3), "pen" denotes the penalty coefficient, while $(Rest)_i$ is the constraint applied to the i-th node. "Pen" was taken into consideration in this study to be at least ten times the maximum stiffness matrix component of the stringer-stiffened shell. The first-order variation of $(Rest)_i$ is given by Eq. (B.4).

$$\delta(Rest)_i = pen * \left[\sum_{m=1,3,\ldots}^{M} u_{mi} + \frac{1}{2}u_{0i} - \frac{\Delta_0}{2}\right] * \delta\left[\sum_{p=1,3,\ldots}^{M} u_{pi} + \frac{1}{2}u_{0i}\right] \tag{B.4}$$

The stiffness of the $i$th node Eq. (B.5) was obtained by expanding Eq. (B.4).

$$\begin{aligned} K^{u,u}_{(p_i)(m_i)} &= pen \\ K^{u,u_0}_{(p_i)(0_i)} &= \frac{1}{2}pen \\ K^{u_0,u}_{(pi)(mi)} &= \frac{1}{2}pen \\ K^{u_0,u_0}_{(0i)(0i)} &= \frac{1}{4}pen \end{aligned} \tag{B.5}$$

The stiffness component of each node is shown in Eq. (B.5), and interactions between the nodes were not taken into account in this study. Through the expansion and simplification of Eq. (B.3), the non-zero components of the external load vector for the third loading case were derived from Eq. (B.6).

$$\begin{Bmatrix} F^{u}_{pi} \\ F^{u_0}_{0i} \end{Bmatrix} = -pen * \begin{Bmatrix} \frac{\Delta_0}{2} \\ \frac{\Delta_0}{4} \end{Bmatrix} \tag{B.6}$$